



Kronoseismology. VI. Reading the Recent History of Saturn's Gravity Field in Its Rings

M. M. Hedman¹, P. D. Nicholson², M. El Moutamid³, and S. Smotherman¹

¹ Physics Department, University of Idaho, Moscow, ID, USA

² Department of Astronomy, Cornell University, Ithaca, NY, USA

³ Cornell Center for Astronomy and Planetary Science, Cornell University, Ithaca, NY, USA

Received 2021 October 1; revised 2022 January 20; accepted 2022 January 20; published 2022 March 11

Abstract

Saturn's C ring contains multiple structures that appear to be density waves driven by time-variable anomalies in the planet's gravitational field. Semiempirical extensions of density wave theory enable the observed wave properties to be translated into information about how the pattern speeds and amplitudes of these gravitational anomalies have changed over time. Combining these theoretical tools with wavelet-based analyses of data obtained by the Visual and Infrared Mapping Spectrometer on board the Cassini spacecraft reveals a suite of structures in Saturn's gravity field with azimuthal wavenumber 3, rotation rates between $804^\circ \text{ day}^{-1}$ and $842^\circ \text{ day}^{-1}$, and local gravitational potential amplitudes between 30 and $150 \text{ cm}^2 \text{ s}^{-2}$. Some of these anomalies are transient, appearing and disappearing over the course of a few Earth years, while others persist for decades. Most of these persistent patterns appear to have roughly constant pattern speeds, but there is at least one structure in the planet's gravitational field whose rotation rate steadily increased between 1970 and 2010. This gravitational field structure appears to induce two different asymmetries in the planet's gravity field, one with azimuthal wavenumber 3 that rotates at roughly $810^\circ \text{ day}^{-1}$ and another with azimuthal wavenumber 1 rotating three times faster. The atmospheric processes responsible for generating the latter pattern may involve solar tides.

Unified Astronomy Thesaurus concepts: [Saturn \(1426\)](#); [Planetary rings \(1254\)](#); [Planetary atmospheres \(1244\)](#); [Planetary interior \(1248\)](#); [Wavelet analysis \(1918\)](#); [Stellar occultation \(2135\)](#); [Solar system gas giant planets \(1191\)](#); [Celestial mechanics \(211\)](#)

1. Introduction

Saturn's rings contain multiple structures that are generated by resonances with asymmetries and oscillations within the planet (Hedman & Nicholson 2013, 2014; French et al. 2016, 2019; Hedman et al. 2019; French et al. 2021). Many of these waves are likely generated by planetary normal mode oscillations, and precise measurements of these oscillation frequencies have already yielded new insights into Saturn's internal structure and rotation rate (Fuller 2014; Mankovich et al. 2019; Mankovich & Fuller 2021). However, there is another class of ring waves that are generated by something happening inside Saturn, but whose exact origins are less clear. One of these waves was first identified in Voyager radio occultation measurements (Rosen et al. 1991), while several others were discovered in stellar occultation data obtained by the Ultraviolet Imaging Spectrometer (UVIS) on board the Cassini spacecraft (Baillié et al. 2011). Most of these features were later identified as three-armed spiral patterns with rotation rates close to Saturn's spin rate, using stellar occultation data obtained by Cassini's Visual and Infrared Mapping Spectrometer (VIMS; Hedman & Nicholson 2014; El Moutamid et al. 2016).⁴ The fact that these patterns appear to track Saturn's rotation strongly suggests that these features are driven by

asymmetries in the planet's gravitational field, but how these asymmetries are generated is still unclear.

Comparing occultation data obtained over the entire course of the Cassini mission reveals that the wavelengths, pattern speeds, and locations of the ring waves are actually time-variable. This implies that the amplitudes and rotation rates of the asymmetries inside the planet that drive these waves are also changing over time. In this paper, we develop new theoretical tools and wavelet-based techniques to translate the observable ring structures into information about how the rotation periods and amplitudes of these anomalies have changed over the past few decades. These analyses show that while some anomalies in the planet's gravitational field persist for up to 40 Earth years, others are much more transient, lasting for less than a decade. These should provide insights into the internal dynamics of giant planets.

The techniques we have developed to interpret these data are somewhat complex and so require both prior motivation and detailed explanation. Section 2 therefore provides a review of the observational data and standard wavelet-based analytical techniques used to identify signals from density waves. This section also discusses how these data and tools provide evidence that certain waves are generated by time-variable perturbations. Section 3 then describes the phenomenological models and analytical techniques needed to translate the observed properties of these structures into quantitative information about the recent history of the perturbations acting on the ring (note that this long section will be most relevant to those interested in how ring structures can act as historical records of transient phenomena). Finally, Section 4 presents the results of applying these techniques to the waves that appear to be generated by asymmetries in the planet's gravitational field,

⁴ The one exception being the wave first noticed in the Voyager data, which is a one-armed spiral with a rotation rate roughly three times Saturn's spin rate. The connection between this wave and the three-armed waves will be discussed in more detail below.



while Section 5 discusses the potential implications of these findings for Saturn’s interior.

2. Background

Prior to discussing the details of the theoretical tools and analytical techniques needed to interpret density wave signals from time-variable perturbations, we first present some evidence that these tools are necessary. This section therefore starts with a brief overview of the available observational data used in this study (Section 2.1), followed by a review of the expected properties of standard density waves and the existing wavelet-based techniques for isolating and quantifying these patterns (Section 2.2). Finally, Section 2.3 shows that these data and tools provide evidence that certain ring structures are generated by forces with time-variable amplitudes or frequencies.

2.1. Observational Data

As with our previous studies of wave-like patterns in Saturn’s rings, this investigation will utilize stellar occultation data obtained by the VIMS instrument on board the Cassini Spacecraft (Brown et al. 2004). While VIMS normally obtained spatially resolved spectra of various targets, this instrument could also repeatedly measure the spectrum of a star as the planet or its rings passed between the star and the spacecraft. In this occultation mode, a precise time stamp was appended to each spectrum to facilitate reconstruction of the observation geometry.

Consistent with our previous analyses, here we will only consider data obtained at wavelengths between 2.87 and 3.00 μm , where the rings are especially dark and so provide a minimal background to the stellar signal. In addition, we use information from the appropriate SPICE kernels (Acton 1996), as well as the timing information encoded with the occultation data, to compute both the radius and inertial longitude in the rings that the starlight passed through. Note that the information encoded in these kernels has been determined to be accurate to within 1 km, and fine-scale adjustments based on the positions of circular ring features enable these estimates to be refined to an accuracy of order 150 m. For this analysis, we use the latest estimates of these offsets from French et al. (2017).

Table 1 provides a list of the occultations that will be considered for this study, which are all the occultations with suitable resolutions and signal-to-noise ratios that cover the region between 83,000 and 90,000 km from Saturn’s center, and therefore contain all the density waves that appear to be generated by asymmetries in the planet’s gravity field, along with a few three-armed spiral waves generated by Saturn’s moons, which are useful bases for comparison. Note that these observations fall into three distinct epochs: 2008–2009, 2012–2014, and 2016–2017. These three epochs are separated by multiyear gaps where the spacecraft’s trajectory did not allow it to observe occultations of the rings. For the following analyses, we will analyze data from these three epochs separately in order to document time-variable structures.

Since the VIMS instrument has a highly linear response function (Brown et al. 2004), the raw data numbers returned by the spacecraft are directly proportional to the apparent brightness of the star. We can therefore estimate the transmission through the rings T as simply the ratio of the observed signal at

a given radius to the average signal in regions outside the rings. From this transmission, we can compute the ring’s optical depth τ using the standard formula $\tau = -\ln(T)$. Both T and τ depend on the observation geometry, but for relatively low optical depth regions, like the middle C ring, we can define the normal optical depth $\tau_n = \tau |\sin(B)|$ (with B being the ring opening angle to the star), which should be nearly independent of B for all the occultations considered here. Note that in order to facilitate the wavelet analysis of these profiles (which requires combining data from multiple occultations), we interpolate the transmission values T from each occultation onto a regular grid of radii, with a spacing of 100 m, before converting the resulting profiles to normal optical depth τ_n .

2.2. Review of Wavelet-based Tools for Analyzing Standard Density Waves

Wavelet transformations have proven to be extremely useful tools for characterizing the wave-like patterns in the rings (see Tiscareno & Hedman 2018 for a recent review). This particular analysis will build upon the wavelet-based analytical tools that have previously been developed to identify and characterize density waves in Saturn’s rings (Hedman & Nicholson 2014, 2016; Hedman et al. 2019). For the sake of completeness and clarity, this section provides a brief review of the basic properties of the standard spiral density waves in Saturn’s rings, as well as the wavelet-based statistics that can be used to identify and characterize the signals associated with these waves.

A standard spiral density wave is a structure that consists of $|m|$ tightly wrapped arms and that rotates at a pattern speed Ω_p (Shu 1984; Nicholson et al. 1990; Tiscareno et al. 2007). These patterns are typically generated at resonant locations r_L , where the ring particles’ orbital mean motion n_L and radial epicyclic frequency κ_L satisfy the following relationship:

$$m(n_L - \Omega_p) = \kappa_L. \quad (1)$$

As in previous works, we allow m to be a signed quantity in this expression, so that $m > 0$ means that the pattern speed is slower than the mean motion (corresponding to an inner Lindblad resonance or ILR), while $m < 0$ means that the pattern speed is faster than the mean motion (corresponding to an outer Lindblad resonance or OLR). These patterns produce variations in the local surface mass density that generate variations in the ring’s optical depth τ with radius r , longitude λ , and time t of the following form:

$$\tau = \tau_0 \Re[1 + A(r)e^{i[\phi_r(r) + |m|(\lambda - \Omega_p t) + \varphi_0]}], \quad (2)$$

where τ_0 and φ_0 are constants, $A(r)$ is a slowly varying function of radius, and $\phi_r(r)$ is the radius-dependent part of the wave’s phase, which has the following form at sufficiently large distances from the resonant radius r_L (so long as $m \neq 1$; Shu 1984):

$$\phi_r(r) = \frac{3|m - 1|M_p(r - r_L)^2}{4\pi\sigma_0 r_L^4}, \quad (3)$$

where σ_0 is the ring’s surface mass density and M_p is the planet’s mass. This structure therefore has a radial wavenumber $k = |\partial\phi_r/\partial r|$ that varies linearly with radius.

Wavelet transforms provide a way to isolate and quantify these sorts of quasiperiodic signals. More specifically, a wavelet transformation is applied to each occultation profile using the IDL wavelet routine (Torrence & Compo 1998)

Table 1
The Occultations Used in This Study

Name ^a	Date	B^b	λ_*^c	λ^d	Name	Date	B^b	λ_*^c	λ^d	Name	Date	B^b	λ_*^c	λ^d
RCas065i	2008-112	56.0	222.9	37.7-40.5	betPeg172i	2012-266	31.7	212.3	309.3-311.6	alpSco241e	2016-243	-32.2	118.5	17.7-23.9
gamCru078i	2008-209	-62.3	50.7	181.2-182.1	lamVel173i	2012-292	-43.8	0.3	144.8-150.1	alpSco243e	2016-267	-32.2	118.5	16.6-22.6
gamCru079i	2008-216	-62.3	50.7	179.5-180.6	WHya179i	2013-019	-34.6	75.7	141.1-145.2	alpSco245e	2016-287	-32.2	118.5	14.9-21.5
RSCnc080i	2008-226	30.0	10.8	75.9-85.8	WHya180i	2013-033	-34.6	75.7	141.6-145.7	gamCru245e	2016-286	-62.4	50.7	265.6-276.3
RSCnc080e	2008-226	30.0	10.8	125.9-135.9	WHya181i	2013-046	-34.6	75.7	141.6-145.7	gamCru255i	2017-001	-62.4	50.7	147.0-147.3
gamCru082i	2008-238	-62.3	50.7	178.2-179.4	muCep185e	2013-090	59.9	184.5	46.4-52.6	gamCru264i	2017-066	-62.4	50.7	145.2-145.5
RSCnc085i	2008-263	30.0	10.8	79.9-93.4	WHya186e	2013-103	-34.6	75.7	296.5-297.9	lamVel268i	2017-094	-43.8	0.3	135.0-136.0
RSCnc085e	2008-263	30.0	10.8	117.9-131.4	gamCru187i	2013-112	-62.4	50.7	144.6-150.0	gamCru268i	2017-095	-62.4	50.7	144.1-144.4
gamCru086i	2008-268	-62.3	50.7	177.2-178.5	gamCru187e	2013-112	-62.4	50.7	227.3-232.7	VYCMa269i	2017-100	-23.4	337.4	197.2-203.5
RSCnc087i	2008-277	30.0	10.8	82.0-99.3	WHya189e	2013-132	-34.6	75.7	295.3-296.7	gamCru269i	2017-102	-62.4	50.7	144.0-144.3
RSCnc087e	2008-277	30.0	10.8	111.9-129.2	RCas191i	2013-149	56.0	222.9	295.3-296.5	gamCru276i	2017-148	-62.4	50.7	144.1-144.2
gamCru089i	2008-290	-62.3	50.7	177.0-178.2	muCep191i	2013-148	59.9	184.5	289.2-290.0	gamCru291i	2017-245	-62.4	50.7	130.6-130.8
gamCru093i	2008-320	-62.3	50.7	206.7-207.9	muCep193i	2013-172	59.9	184.5	289.4-290.2	gamCru292i	2017-251	-62.4	50.7	129.8-130.0
gamCru094i	2008-328	-62.3	50.7	191.7-191.8	RCas194e	2013-186	56.0	222.9	84.5-85.8					
gamCru100i	2009-012	-62.3	50.7	220.7-223.4	2Cen194i	2013-189	-40.7	75.6	147.1-152.3					
gamCru102i	2009-031	-62.3	50.7	220.4-223.1	2Cen194e	2013-189	-40.7	75.6	230.4-235.6					
betPeg104i	2009-057	31.7	212.3	343.4-346.1	RLyr198i	2013-289	40.8	148.1	261.6-263.1					
RCas106i	2009-081	56.0	222.9	71.8-83.9	RLyr199i	2013-337	40.8	148.1	230.3-235.5					
alpSco115i	2009-209	-32.2	118.5	158.9-162.0	RLyr200i	2014-003	40.8	148.1	256.6-258.5					
					RLyr202e	2014-067	40.8	148.1	56.2-59.9					
					L2Pup205e	2014-175	-41.9	332.3	222.1-227.9					
					RLyr208e	2014-262	40.8	148.1	46.0-51.1					

Notes.

^a The occultation name, consisting of the star name, the Cassini orbit number, and a designation of the occultation being ingress (i) or egress (e).

^b The ring opening angle to the star, in degrees.

^c The inertial longitude of the star in the sky, in degrees from the ring's ascending node on J2000.

^d The observed range of inertial longitudes in the rings between 83,000 and 90,000 km, in degrees.

with a Morlet mother wavelet and parameter $\omega_0 = 6$. This specific wavelet transformation is essentially a localized Fourier transformation, yielding the complex wavelet $\mathcal{W}_i = \mathcal{A}_i e^{i\Phi_i}$, where \mathcal{W}_i , \mathcal{A}_i , and Φ_i are all functions of both radius r and radial wavenumber k . This wavelet transform of an individual occultation profile reveals quasi-sinusoidal patterns associated with spiral waves as locations containing elevated amplitudes at specific wavenumbers, with the signal from a standard density wave appearing as a diagonal band in plots of the wavelet amplitude versus k and r (Tiscareno & Hedman 2018; see also Figure 11).

More importantly, wavelet transforms of multiple occultations can be combined to isolate signals from specific waves with particular values of m and Ω_p . This is accomplished by using the observed longitude λ_i and observation time t_i for each occultation to compute the phase parameter $\phi_i = |m|[\lambda_i - \Omega_p t_i]$. This quantity is then used to calculate the phase-corrected wavelet:

$$\mathcal{W}_{\phi,i} = \mathcal{W}_i e^{-i\phi_i} = \mathcal{A}_i e^{i(\Phi_i - \phi_i)}. \quad (4)$$

Note that Φ_i is equivalent to the phase of the sinusoidal optical depth variations associated with a wave (see Equation (2)), so for any wave with the specified values of $|m|$ and Ω_p , the phase difference $\Phi_i - \phi_i = \phi_i(r) + \varphi_0$ for every occultation. Since this difference should be the same for all of the occultation profiles, the average phase-corrected wavelet

$$\langle \mathcal{W}_\phi \rangle = \frac{1}{N} \sum_{i=1}^N \mathcal{W}_{\phi,i} \quad (5)$$

will be nonzero for such a wave, while any signal without these properties will average to zero. Thus, only the desired signal should remain in the power of the average phase-corrected wavelet

$$\mathcal{P}_\phi(r, k) = |\langle \mathcal{W}_\phi \rangle|^2 = \left| \frac{1}{N} \sum_{i=1}^N \mathcal{W}_{\phi,i} \right|^2, \quad (6)$$

while all other signals are only seen in the average wavelet power

$$\bar{\mathcal{P}}(r, k) = \langle |\mathcal{W}_\phi|^2 \rangle = \frac{1}{N} \sum_{i=1}^N |\mathcal{W}_{\phi,i}|^2. \quad (7)$$

The ratio of these two powers $\mathcal{R}(r, k) = \mathcal{P}_\phi / \bar{\mathcal{P}}$ (which ranges between 0 and 1; see Hedman & Nicholson 2016) therefore provides a measure of how much of the signal is consistent with the assumed m and Ω_p . Hence, for any given value of m , we can compute \mathcal{P}_ϕ and \mathcal{R} for a range of pattern speeds, and determine the true pattern speed as the one that maximizes these statistics.

2.3. Evidence that Planet-generated Density Waves are Generated by Time-variable Forces

Preliminary examinations of the waves generated by asymmetries in the planet's gravitational field provide two lines of evidence that the forces responsible for generating these waves are time-variable. First of all, direct comparisons of high-quality occultation profiles obtained from the three different parts of the Cassini Mission reveal that the strongest waves with pattern speeds close to Saturn's rotation rate visibly change over timescales of a few years. Second, wavelet

analyses of these same structures reveal that they do not have the fixed pattern speeds expected for standard density waves. This latter aspect of these density waves can also be observed in several weaker waves with pattern speeds close to Saturn's rotation rate. These variable pattern speeds are indirect evidence for time-dependent perturbations acting on the ring, because this behavior is inconsistent with the expected response of the rings to a strictly periodic perturbing force.

Figure 1 shows optical depth profiles of the two waves that were designated W84.82 and W84.86 by Hedman & Nicholson (2014). These waves are located around 84,825 and 84,865 km from Saturn's center, and were found to be three-armed spirals with pattern speeds of 833.5 day^{-1} and 833.0 day^{-1} , respectively, comparable to the rotation rate of Saturn's equatorial jet (Hedman & Nicholson 2014). Quasiperiodic optical depth variations associated with both waves can be seen in all three profiles, but it is also clear that over the course of the Cassini mission, the wavelengths of both these patterns shortened. Furthermore, the locations of the signals shift slightly outward over time (this is clearer for the stronger W84.82 pattern). Both these trends are in stark contrast to the observed behavior of standard density waves generated by most satellites or by normal modes inside the planet, which remain at a fixed location and maintain a fixed wavelength at any given radius.

The closest analogs to these time variations are found in the waves generated by the co-orbital moons Janus and Epimetheus. These two moons undergo rapid changes in their semimajor axes and orbital periods every four years that cause sudden changes in the locations of their resonances in the rings. Many of the density waves generated at these resonances show unusual morphologies that can best be understood as superpositions of "wave fragments," each of which corresponds to a part of a standard density wave generated when the resonance was at a particular location (Tiscareno et al. 2006). According to this model, each wave fragment is generated at a particular resonant location, and then moves outward at the appropriate group velocity for density perturbations in the rings (Shu 1984):

$$v_g = \pi G \sigma_0 / \kappa, \quad (8)$$

where G is the universal gravitational constant, σ_0 is the background ring surface mass density, and κ is the local radial epicyclic frequency.

W84.82 and W84.86 look like they can also be regarded as isolated "wave fragments." For one, they are clearly moving outward, which is the correct direction for a wave fragment generated by an ILR with a pattern speed slower than the local mean motion (Shu 1984; Tiscareno et al. 2006). Furthermore, for this part of the ring, the surface mass density was estimated to be around $2\text{--}4 \text{ g cm}^{-2}$ (Hedman & Nicholson 2014; but see below for evidence that this was an overestimate), and $\kappa \simeq 1225 \text{ day}^{-1}$, so the expected group velocity should be between 0.5 and 1 km yr^{-1} , which is roughly consistent with the observed radial shifts of the wave locations between the profiles shown in Figure 1, which amount to a few kilometers over 7 yr. Furthermore, the observed decrease in wavelength and increase in wavenumber is consistent with the expected behavior of a wave fragment moving away from the resonant radius (see Section 3.1).

A rather different sort of time variability is found with the wave designated W86.40, which Hedman & Nicholson (2014)

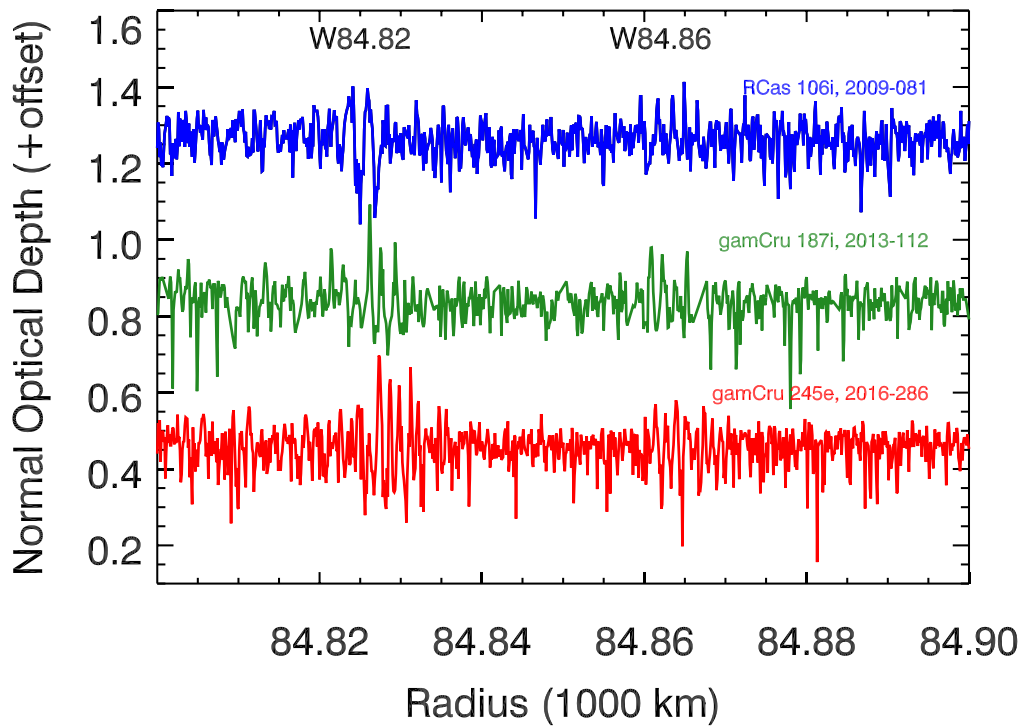


Figure 1. Comparisons of three high-quality normal optical depth (τ_n) profiles obtained from three different times during the Cassini mission (the year and day numbers are provided in the colored labels), focusing on the waves designated W84.82 and W84.86. In this case, the wavelengths of the wave patterns around 84,825 and 84,865 km clearly shorten over the course of the Cassini mission. The wave packet around 84,825 km also steadily moves outward over time.

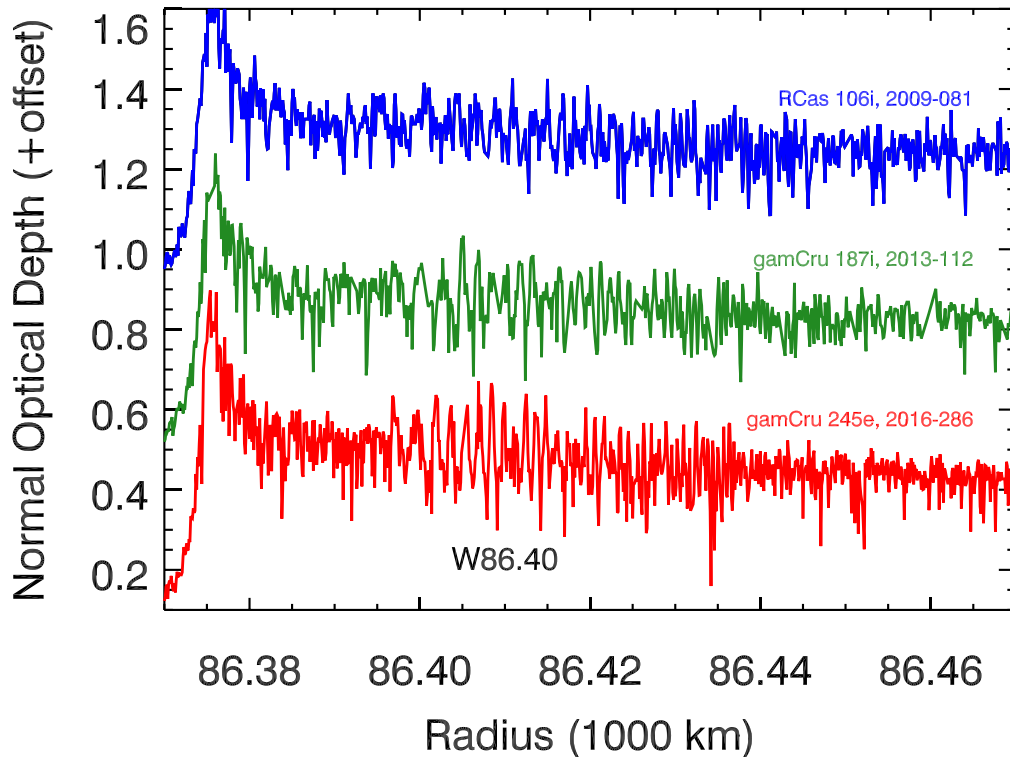


Figure 2. Comparisons of three high-quality normal optical depth (τ_n) profiles obtained from three different times during the Cassini mission (the year and day numbers are provided in the colored labels), focusing on the wave designated W86.40. The wavelength of this pattern around 86,410 km clearly shortens over the course of the Cassini mission. Furthermore, the wave appears to be shifting inward over time, with the region of the highest-amplitude variations shifting from about 86,420 km to around 86,405 km during this 8 yr period.

found was a three-armed spiral pattern with a pattern speed of $810^{\circ}4 \text{ day}^{-1}$, a speed that overlaps with the rotation rates of Saturn’s westward jets. Figure 2 shows three high-quality

profiles of this wave from the three different epochs of the Cassini Mission. In this case, the wavelength of the pattern at any given radius again declines over time (most obviously

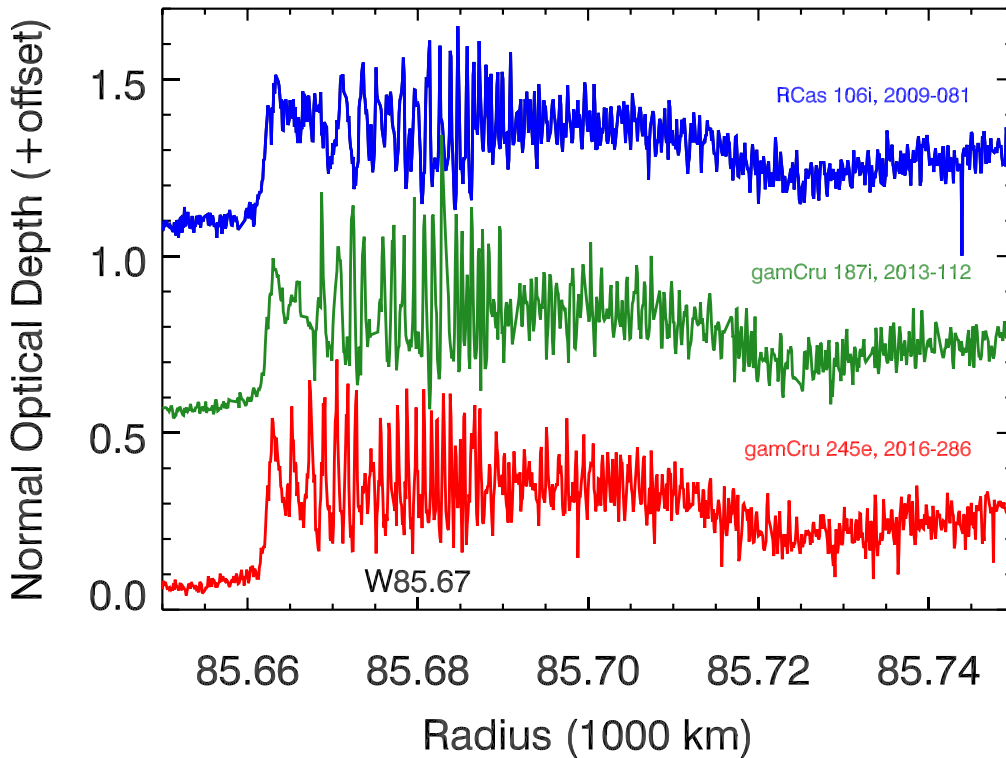


Figure 3. Comparisons of three high-quality normal optical depth (τ_n) profiles obtained from three different times during the Cassini mission (the year and day numbers are provided in the colored labels), focusing on the wave designated W85.67. The wavelength of this pattern around 85,670 km clearly shortens over the course of the Cassini mission. Furthermore, the wave appears to be shifting inward over time, with the leftmost part of the wave being much closer to the plateau edge at 85,660 km by the end of the Cassini Mission.

around 86,410 km). In addition, it appears that the wave as a whole could be moving *inward* over time, because the part of the wave with the largest-amplitude optical depth variations shifts from around 86,420 km in 2009 to around 86,405 km in 2016.

The behavior of W86.40 is highly reminiscent of another wave that was previously identified as time-variable. This wave, designated W85.67, was identified as a one-armed spiral pattern with a pattern speed of $2430^\circ \text{day}^{-1}$ (Hedman & Nicholson 2014). This is the only one of these variable waves that was also visible in the Voyager radio occultation, and comparisons between the Voyager data and the early Cassini data clearly showed that the wave as a whole was moving inward over time. Figure 3 demonstrates that the inward motion of this wave continued up through the end of the Cassini mission (note that the inner edge of the wave gets progressively closer to the sharp inner edge of the plateau). Hedman & Nicholson (2014) interpreted this pattern’s evolution as evidence that the periodic perturbation frequency responsible for generating this wave was slowly increasing over time, causing the resonant location to drift steadily closer to the planet. Since W86.40 shows a similar evolution over time as W85.67, it seems likely that the periodic force responsible for generating this wave also has a frequency that is increasing over time, causing the wave to steadily move inward.

While visual inspection of individual high-quality occultation profiles is sufficient to document some aspects of the temporal variability of these waves, wavelet analysis reveals another unusual aspect of these waves: different parts of the waves do not have a single, constant pattern speed. This is most easily demonstrated by considering only the data from Epoch 1 (2008–2009). This epoch contains enough occultations to

ascertain the pattern speeds of these structures, while also covering a sufficiently short period of time that the variations in the pattern’s wavelength do not strongly suppress the signals in the phase-corrected average wavelet.

Figure 4 illustrates the typical behavior of most of the density waves in the rings. The top panel shows the optical depth profile of the wave designated W84.64 in the middle C ring, which is generated by a planetary normal mode. The bottom panel shows the results of a wavelet analysis of the Epoch 1 occultations, assuming the pattern has $m = -2$. The plot shows the peak value of the wavelet power ratio \mathcal{R} for wavelengths between 0.2 and 2 km as a function of ring radius and assumed pattern speed. The pattern speed is expressed as an offset from the nominal pattern speed $\delta\Omega_p$, as well as the corresponding offset in the resonant radius δr used to compute that pattern speed offset (see Equation (1)). Both the nominal pattern speed and resonant radius are given at the top of the figure. In this specific case, the signal from the wave forms a dark horizontal band that occupies roughly the same radial range as the wave itself. This signal falls along the horizontal line that corresponds to $\delta r = \delta\Omega_p = 0$, which means that the entire wave has the same pattern speed of $1860.752 \text{ day}^{-1}$. This is consistent with the signals seen from other waves generated by planetary normal modes and by satellites with constant mean motions (Hedman & Nicholson 2016; French et al. 2019; Hedman et al. 2019).

If we now turn our attention to the time-variable $m = 3$ waves, we find a very different behavior. To start with, Figure 5 shows a wavelet analysis of the waves W84.82 and W84.86. These two waves produce clear signals in the wavelet transform, and the signals from these two patterns have pattern speeds that correspond roughly to a 30 km separation in

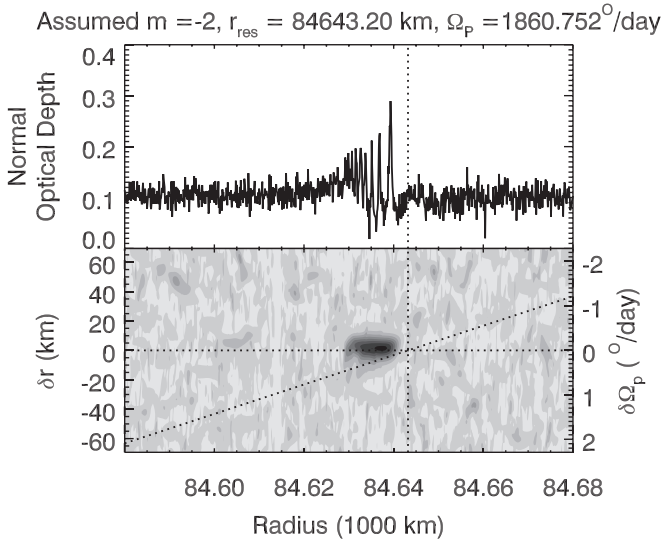


Figure 4. The results of a wavelet analysis of a density wave driven by a planetary normal mode. The top panel shows the normal optical depth (τ_n) profile of the density wave W84.64 from the Rev 106 RCAs occultation. The bottom panel shows the peak value of the wavelet power ratio \mathcal{R} for wavelengths between 0.2 and 2 km for the observations from Epoch 1 as functions of radius and pattern speed. The latter is expressed in terms of offsets in both the assumed pattern speed $\delta\Omega_p$ and resonant radius δr from the nominal values given at the top of the plot. In this case, the entire wave has the same pattern speed, and so the peak signals at all radii fall along a horizontal line. This is a characteristic found in most waves generated by satellites or planetary normal modes.

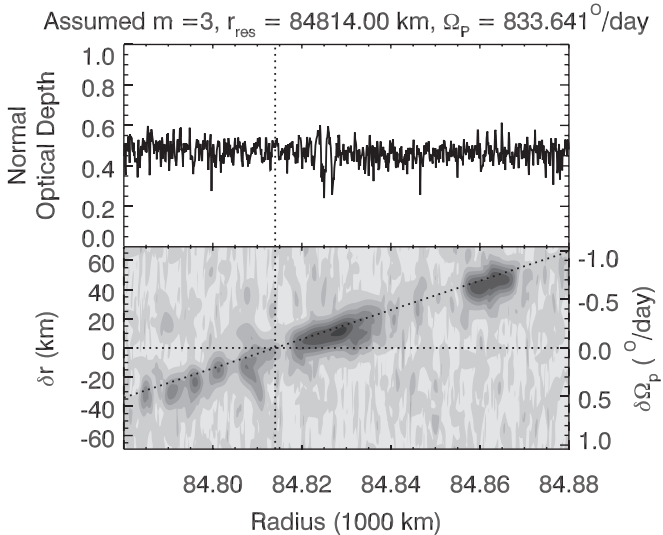


Figure 5. The results of a wavelet analysis of the waves W84.82 and W84.86, showing the same optical depth profile and peak \mathcal{R} data computed in the same way as Figure 4. In this case, not only do the two waves have different pattern speeds, but each wave also shows variations in its pattern speed with radius. These trends are parallel to the diagonal dotted line, which corresponds to the local pattern speed of a wave at that location. Note also that additional wavelet signals are found along this line interior to W84.82, which likely correspond to additional wave fragments not obvious in the profile.

resonant radius, which is consistent with the radial separation of these waves. However, unlike the wave shown in Figure 4, the signal from each of these waves is not a horizontal band, but is instead tilted, indicating that the outer part of each wave has a slower pattern speed than the inner part. Also shown in this plot is a diagonal dotted line that indicates the expected value of the pattern speed given by Equation (1), evaluated at

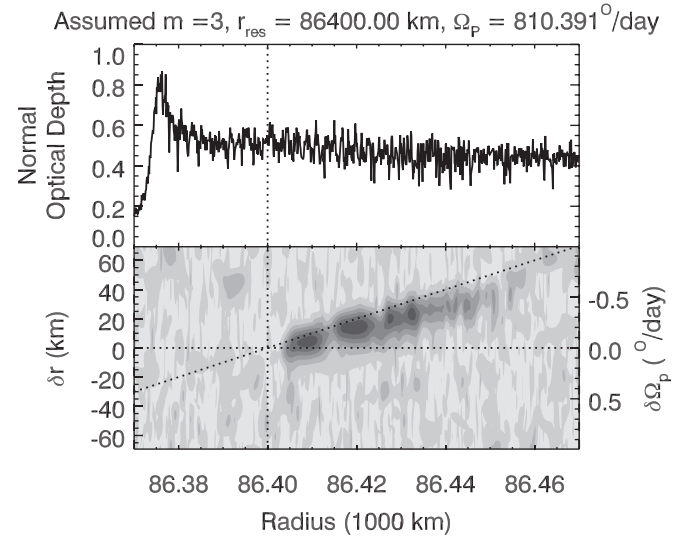


Figure 6. The results of a wavelet analysis of the wave W86.40, showing the same optical depth profile and peak \mathcal{R} data computed in the same way as Figure 4. There are clear variations in the wave's pattern speed with radius that follow a trend similar to the diagonal dotted line that corresponds to the expected local pattern speed. In this case, the peak signals appear to occur at pattern speeds that correspond to a location 10–20 km interior to the observed location.

each radius. The signals from both waves generally follow this trend, although the peak signals consistently occur at pattern speeds $\sim 0.1 \text{ day}^{-1}$ faster than those predicted by Equation (1). (Alternatively, the resonant radius that best explains the rotation of the pattern at each radius is ~ 10 km interior to the observed location.) Furthermore, interior to W84.82, there are a series of weaker signals that fall along this same trend, indicating that there are additional wave fragments that are too weak to be seen in the individual profiles. It appears that these wave fragments all have pattern speeds close to the local resonant value, rather than some fixed speed determined by an external perturbation. This suggests that the perturbations responsible for generating these features are no longer active, consistent with the abovementioned idea that these are freely propagating wave fragments created at some time in the past.

Next, consider the W86.40 wave analysis shown in Figure 6. As mentioned above, this structure appears to be more of a continuous wave than W84.82 and W84.86. However, the wavelet analysis reveals that this wave also does not have a single pattern speed. Again, the parts of the wave at larger radii have lower pattern speeds that correspond to resonant radii further from the planet. Also, between 86,400 and 86,420 km, the pattern speed is again $\sim 0.1 \text{ day}^{-1}$ faster than the local rate, corresponding to a ~ 10 km inward offset in the assumed resonant radius. However, this offset appears to become larger with increasing radius between $\sim 86,420$ and 86,450 km. These variations in the observed pattern speed are again inconsistent with this wave being generated by a strictly periodic perturbing force. However, in this case, the observed temporal variations in the wave itself are less consistent with discrete wave fragments propagating through the rings. Indeed, more detailed analysis of this structure indicates that it is generated by a perturbing force with a continuously changing rotation rate (see Section 4.2). It is also worth noting that the amplitude of the wavelet signal does not follow a smooth trend with radius, but instead has minima at $\sim 86,410$ and $\sim 86,425$ km.

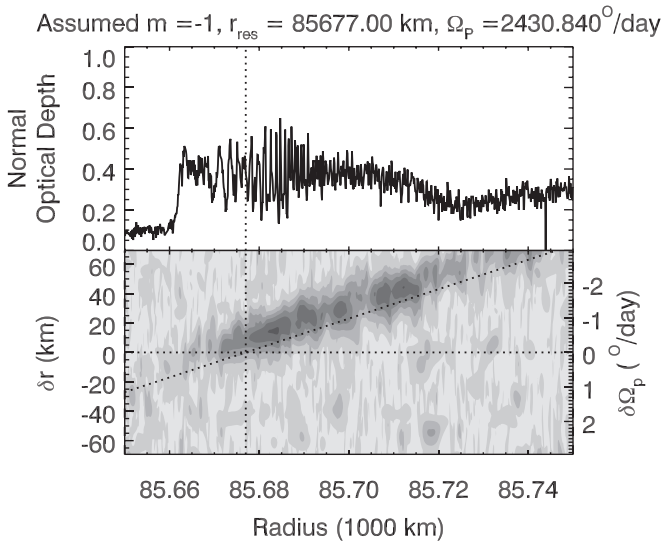


Figure 7. The results of a wavelet analysis of the wave W85.67, showing the same optical depth profile and peak \mathcal{R} data computed in the same way as Figure 4. There are clear variations in the wave’s pattern speed with radius that follow a trend similar to the diagonal dotted line that corresponds to the expected local pattern speed. In this case the peak signals appear to occur at pattern speeds that correspond to a location 10–20 km exterior to the observed location.

It is again interesting to compare the properties of this wave with those of W85.67. As shown in Figure 7, this time-variable wave, despite being a one-armed spiral instead of a three-armed spiral, shows a variable pattern speed with a radial trend very similar to that displayed by W86.40. Again, the parts of the wave further from the planet have slower pattern speeds, but in this case, the pattern speed is $\sim 0.3 \text{ day}^{-1}$ slower than the local pattern speed predicted by Equation (1), which corresponds to a resonant radius that is $\sim 10 \text{ km}$ exterior to the observed location. This difference in behavior between W86.40 and W85.67 can probably be explained by the fact that the pattern speed of W86.40 is slower than the local mean motion (i.e., it is generated by an ILR), while the pattern speed of W85.67 is greater than the local mean motion (i.e., it is generated by an OLR). This means that if the frequency of the disturbing force were constant, W86.40 would naturally propagate outward, while W85.67 would naturally propagate inward (Shu 1984).

Of course, this picture is complicated somewhat by the fact that these waves appear to be generated by time-variable perturbations whose resonance locations appear to be moving inward over time (in fact, W85.67 appears to propagate outward, because the relevant perturbation frequency is changing fast enough that the resonant radius moves inward faster than the wave can propagate; see Hedman & Nicholson 2014). Even so, it is reasonable to expect that the various parts of W85.67 should still be propagating inward, while those of W86.40 should be propagating outward. The pattern speeds for both W86.40 and W85.67 therefore appear to be biased in the direction of where the observed parts of the wave should have come from. The pattern speeds of both these waves may therefore reflect something about their past history.

It is also worth considering the last two $m = 3$ density waves examined by Hedman & Nicholson (2014), W86.58 and W86.59. These waves are harder to discern in individual profiles than W84.82, W84.86, and W86.40, but they can be clearly detected in the wavelet maps, as seen in Figure 8. As with W84.82 and W84.86, it turns out that these two waves are part of an array of weaker signals with a range of different pattern speeds that were

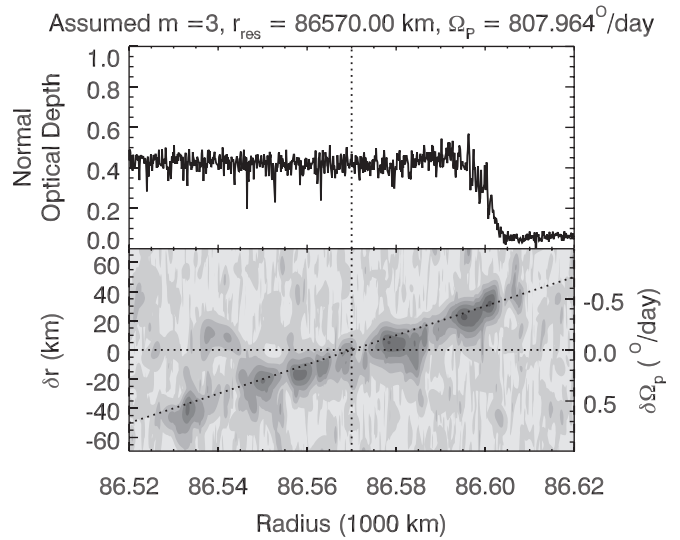


Figure 8. The results of a wavelet analysis of the region around 86.570 km, including the W86.58 and W86.59 waves, showing the same optical depth profile and peak \mathcal{R} data computed in the same way as Figure 4. This region shows signals with a range of pattern speeds, only two of which were previously identified as wave-like.

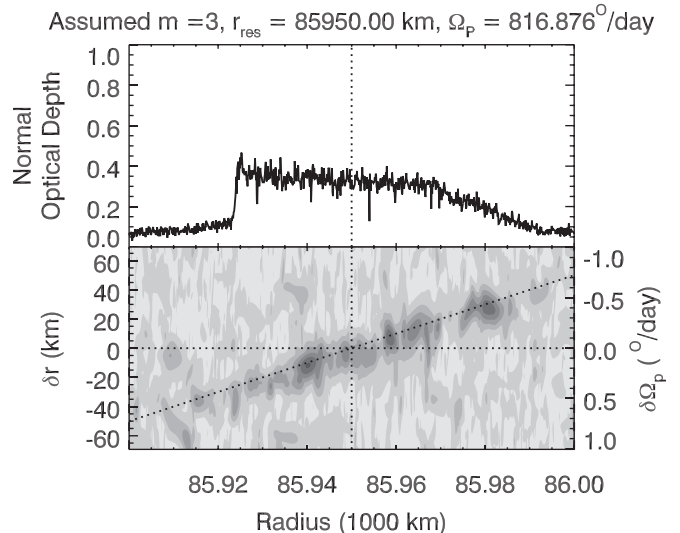


Figure 9. The results of a wavelet analysis of the region around 85.950 km, showing the same optical depth profile and peak \mathcal{R} data computed in the same way as Figure 4. Although there is not an obvious wave in the profile, $m = 3$ signals are visible throughout this region with a range of pattern speeds.

not apparent in individual profiles. In this case, the signals appear to be much more patchy, suggesting that the region between ~ 86.530 and $\sim 86.610 \text{ km}$ contains an array of weak wave fragments.

The above supposition is further supported by the fact that we have found even more of these signals in other parts of the C ring. For example, Figure 9 shows the wavelet analysis for the plateau-like structure centered on 85,950 km. This region was not previously identified as containing wave-like patterns (Baillié et al. 2011), but the wavelet analysis reveals weak three-armed spiral patterns all across this feature. The extended distribution of patterns with a range of pattern speeds again suggests that multiple weak wave fragments are probably the most common three-armed spiral patterns in this region.

Figure 10 provides a general overview of the three-armed spiral patterns in the middle C ring (the one-armed wave W85.67 is not

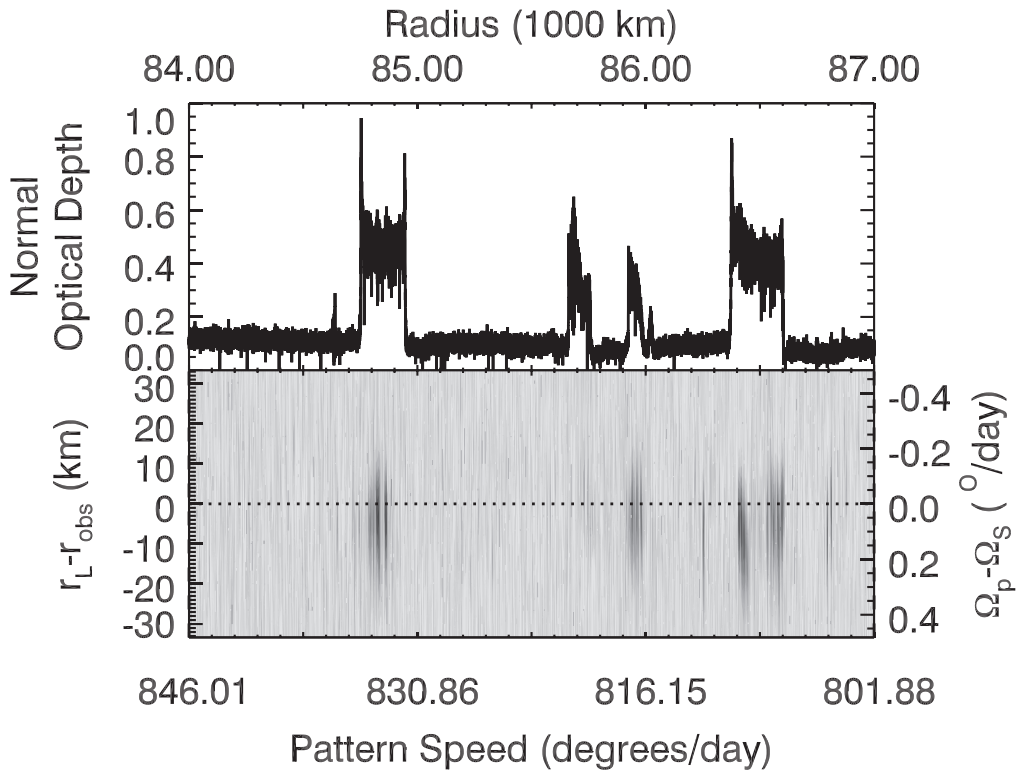


Figure 10. An overview of all of the $m = 3$ patterns in the middle C ring. The top panel shows the normal optical depth profile, while the bottom panel shows the peak value of the wavelet power ratio \mathcal{R} for wavelengths between 0.2 and 2 km for the observations from Epoch 1 as functions of radius and the difference from the expected local pattern speed at each radius.

shown in a similar format because it appears to be unique). In this case, the horizontal line at $r_L - r_{\text{obs}} = 0$ corresponds to where the observed radius equals the resonant radius used to calculate the local pattern speed and phase correct the data. Note that all of the $m = 3$ signals fall around 10–20 km below this line, corresponding to pattern speeds 0.1 day^{-1} faster than the expected local rate, which is consistent with the prior plots. This plot also highlights the curious fact that the strongest signals are mostly—but not exclusively—found within the plateaux at 84,800, 85,950, and 86,500 km (note that the $m = -1$ wave W85.67 is also located within the plateaux at 85,700 km). However, there are a few additional isolated $m = 3$ signals, most prominently around 86,300 and 86,800 km, that are not located within plateaux.

3. Methods

While inspection of selected optical depth profiles and wavelet transforms provide evidence that the perturbations responsible for these structures are time-variable, different techniques are needed to quantify how the amplitudes and frequencies of these perturbing forces have changed over time. For one, we need a theoretical framework for interpreting the morphology of ring waves driven by periodic forces with time-variable amplitudes and frequencies. In addition, we need explicit procedures for translating the observed wave properties into relevant information about the history of the forces acting on the ring.

Fortunately, we have been able to develop a phenomenological model for density waves generated by time-variable forces. This model allows us to directly convert the observed wavenumbers of the patterns in the rings into estimates of when those structures were created, while the locations of these patterns can be translated into estimates of the original resonant radius and thus perturbation frequency, provided we have a reasonable estimate of

the local surface mass density of the rings. These mappings enable us to translate the wavelet parameters \mathcal{P}_ϕ and \mathcal{R} into maps of the perturbation strength as functions of time and pattern speed that can be calibrated against known satellite density waves.

These theoretical models and analytical techniques are described in detail below because they can provide a useful general framework for interpreting evolving structures in planetary rings. First, Section 3.1 discusses our phenomenological model, which predicts a robust connection between a wave pattern’s current wavenumber and its formation time. This basic theory is then validated in Section 3.2 by examining density waves generated by moons with known time-variable orbits. Next, Section 3.3 describes how this theory can be used to translate maps of \mathcal{P}_ϕ and \mathcal{R} into estimates of the strength and rotation rates of the gravitational anomalies as a function of time. Note that this process requires estimating the ring’s surface mass density by comparing observations made at different times, and that it uses nearby satellite-driven waves to normalize the perturbation amplitudes. Finally, Section 3.4 applies these procedures to satellite-driven density waves in order to validate our methods.

Readers more interested in what this analysis reveals about the recent history of the planet’s gravitational field should feel free to proceed directly to the last subsection, which also contains illustrative examples of the maps we will use to document the recent history of the perturbations acting on the rings.

3.1. A Phenomenological Model for Density Waves Generated by Time-variable Forces

Standard theories of density waves assume that the relevant perturbation forces have fixed frequencies and amplitudes (see, e.g., Shu 1984). There is currently no detailed theoretical model for how ring material should respond to transient periodic

perturbing forces, and rigorously extending existing theories to such situations is beyond the scope of this work. Thus, we will instead develop a phenomenological model that enables us to make reasonably secure estimates of when these waves were originally generated and their initial perturbation frequencies/pattern speeds.

This model is based upon earlier work by Tiscareno et al. (2006) that treated the density waves generated by Janus and Epimetheus as a set of wave fragments that propagate at fixed speeds from where they were generated. Here, we posit that, at some time in the past, a periodic perturbing force started to generate a density wave in the rings, but at some later time that force either disappeared or changed frequency, leaving a wave fragment that propagates away from its original location at a rate given by the local group velocity (see Equation (8)) and has a wavelength that becomes progressively shorter, while its pattern speed remains close to the local rate predicted by Equation (1). Furthermore, we will show that these waves have a radial wavenumber that is proportional to the time that has elapsed since the wave was created, and a location that depends on both that elapsed time and the ring's surface mass density.

3.1.1. General Framework and Notation

In order to properly quantify the evolution of the location and wavelength of these patterns, we need a generic picture for density wave-like structures that does not assume the pattern has a fixed pattern speed imposed by an outside force. However, for the sake of simplicity, we can still assume that the ring particles at each semimajor axis a follow a (rotating) streamline with m -fold symmetry, so that the radial location of the streamline r can be written as the following function of (inertial) longitude λ and (implicitly) time t :

$$r = a - A_e(a) \cos[|m|(\lambda - \phi_0(a, t))], \quad (9)$$

where A_e parameterizes the amplitude of the radial motions and ϕ_0 gives the pattern's phase. In general, ϕ_0 can depend on time (yielding a rotating pattern), and both A_e and ϕ_0 can depend on semimajor axis a , leading to variations in the distance between adjacent streamlines that correspond to variations in the ring's surface density. More specifically, the surface mass density σ in such a situation can be written in the following form:

$$\sigma(a, \lambda, t) = \frac{\sigma_0}{\partial r / \partial a}, \quad (10)$$

where σ_0 is the unperturbed surface mass density. The denominator of this expression can be evaluated from Equation (9), which in general gives:

$$\begin{aligned} \frac{\partial r}{\partial a} &= 1 - \frac{\partial A_e}{\partial a} \cos[|m|(\lambda - \phi_0)] \\ &+ A_e |m| \frac{\partial \phi_0}{\partial a} \sin[|m|(\lambda - \phi_0)]. \end{aligned} \quad (11)$$

For standard density waves, we can assume that A_e is a sufficiently smooth function of a so that the second term in the above expression can be ignored, which means

$$\frac{\partial r}{\partial a} \simeq 1 + A_e |m| \frac{\partial \phi_0}{\partial a} \sin[|m|(\lambda - \phi_0)]; \quad (12)$$

and so long as A_e is sufficiently small, the surface mass density has the following form:

$$\sigma(a, \lambda, t) = \sigma_0 - \sigma_0 A_e |m| \frac{\partial \phi_0}{\partial a} \sin[|m|(\lambda - \phi_0)]. \quad (13)$$

The surface mass density therefore has sinusoidal density variations in both the radial and the azimuthal directions. However, we still need to show that the density variations in the radial direction correspond to sensible wave-like structures, and that the entire pattern rotates at a sensible rate. To do this, consider the phase of these variations:

$$\phi(a, \lambda, t) = |m|[\lambda - \phi_0(a, t)]. \quad (14)$$

By construction, this pattern must have an azimuthal wavenumber $|m|$. However, the pattern speed and radial wavenumber of the wave are determined by derivatives of ϕ_0 . Specifically, the radial wavenumber is the radial derivative of the phase at a fixed time t :

$$k(a, t) = \left. \frac{\partial \phi}{\partial a} \right|_t = -|m| \left. \frac{\partial \phi_0}{\partial a} \right|_t; \quad (15)$$

while the pattern speed is the time derivative of the phase at a fixed semimajor axis a , divided by $-|m|$:

$$\Omega_p(a, t) = - \left. \frac{1}{|m|} \frac{\partial \phi}{\partial t} \right|_a = \left. \frac{\partial \phi_0}{\partial t} \right|_a. \quad (16)$$

Hence, we need to determine how ϕ_0 depends on semimajor axis and time. For the sake of concreteness, we will here consider three different situations: freely evolving spiral patterns, forced density waves with a common pattern speed, and, finally, density wave fragments that were initially generated like normal density waves but then propagate freely through the rings.

3.1.2. Freely Evolving Spiral Patterns

First, consider a freely evolving spiral pattern that arises from a situation where the streamlines at all radii are initially aligned with each other (i.e., $\phi_0 = 0$ for all a at some time $t = 0$).⁵ This relatively simple arrangement cannot persist indefinitely because the particles can only follow closed $|m|$ -fold symmetric streamlines if those streamlines rotate at a rate that depends on the radial location in the ring. For the sake of clarity, we will denote this streamline pattern rotation rate as Ω_s in order to distinguish it from the observed pattern speed of the wave. For a massless ring, Ω_s must satisfy the following expression:

$$m(n(a) - \Omega_s(a)) = \kappa(a), \quad (17)$$

where $n(a)$ and $\kappa(a)$ are the particles' mean motion and radial epicyclic frequency, respectively. This particular expression ensures that the time it takes the particle to go around the rotating pattern once (i.e., $2\pi/|\Omega_s - n|$) is an integer multiple of the time between two pericenter passages (i.e., $2\pi/\kappa$).

⁵ In principle, we could allow ϕ_0 to be an arbitrary function of a at this time, but such complications are not particularly informative here.

Since $\Omega_s(a)$ is the local free rotation rate of the streamlines, this means that the phase is simply

$$\phi_0 = \int_0^t \Omega_s(a) dt' = \Omega_s(a)t, \quad (18)$$

which means that in this case the wave's pattern speed is equal to the local streamline rotation rate:

$$\Omega_p(a, t) = \Omega_s(a). \quad (19)$$

Meanwhile, the radial wavenumber of the pattern is

$$k(a, t) = -|m| \frac{\partial \phi_0}{\partial a} \Big|_t = -|m| \frac{\partial \Omega_s}{\partial a} t, \quad (20)$$

and so the wavenumber increases linearly with time. To obtain a more explicit expression for this wavenumber, we can note that to first order $n(a) \simeq \kappa(a) \simeq \sqrt{GM_P/a^3}$, where G is the fundamental gravitational constant and M_P is the planet's mass. In this case, we have

$$\Omega_s = n - \kappa/m \simeq \frac{m-1}{m} \sqrt{\frac{GM_P}{a^3}}, \quad (21)$$

and so the derivative is

$$\frac{\partial \Omega_s}{\partial a} \simeq -\frac{3(m-1)}{2m} \sqrt{\frac{GM_P}{a^5}}. \quad (22)$$

This yields the following expression for the wavenumber of a freely evolving spiral pattern:

$$k(a, t) \simeq \frac{3}{2} |m-1| \sqrt{\frac{GM_P}{a^5}} t. \quad (23)$$

So in this case, the radial wavenumber increases with time at a linear rate that just depends on the feature's location and the planet's mass.

A reasonable concern about the above calculation is that the pattern speed of the observed $m=3$ waves are roughly 0.1 day^{-1} faster than the expected value of Ω_s from Equation (17) (see Figures 5 and 6), and the observed pattern speeds for the $m=-1$ wave are about 0.3 day^{-1} below the expected value of Ω_s (see Figure 7). However, these offsets can be explained by realizing that Equation (17) neglects the orbital perturbations due to the ring's own self-gravity. The gravity of the rings can be incorporated into the above calculation by considering the standard dispersion relation for density waves (Shu 1984), which modifies the equation for the streamline rotation rate Ω_s into the following form:

$$(m\Omega_s - mn)^2 = \kappa^2 - 2\pi G\sigma_0 |k|, \quad (24)$$

where σ_0 is the ring's surface mass density and k is the radial wavenumber of the pattern. This reduces to Equation (17) when σ_0 approaches zero, and so long as $2\pi G\sigma_0 k \ll \kappa^2$, the last term in the above equation can be treated as a small perturbation. In this case, we can solve for Ω_s , which to first order in σ_0 becomes

$$\Omega_s \simeq n - \frac{\kappa}{m} + \frac{\pi G\sigma_0}{m\kappa} |k|. \quad (25)$$

As before, Ω_s turns out to be equal to the observed pattern speed of the wave, which is now slightly different from the value predicted by Equation (17). For the waves with $m=3$, the extra

term causes the real pattern speed to be slightly higher than the expected speed, while for the $m=-1$ wave, this term causes the real pattern speed to be slightly lower than the expected speed, both of which are consistent with the observed wave. Furthermore, if we assume a value of $\kappa \simeq 1220^\circ \text{ day}^{-1}$, which is appropriate for this part of the C ring, as well as $\sigma_0 \simeq 1 \text{ g cm}^{-2}$ (see Section 3.3 below) and $k=2\pi/1 \text{ km}$, then we find the correction term is $+0.09 \text{ day}^{-1}$ for the $m=3$ waves and -0.26 day^{-1} for the $m=-1$ wave, both of which are consistent with the observed offsets in the pattern speeds shown in Figures 5–7. These slight changes in the pattern speed cause comparably small changes in the rate at which the wavenumber increases over time. For the sake of simplicity, these small changes in the winding rate will be neglected from here on.

3.1.3. Resonantly Forced Waves

Next, consider a density wave driven by a (first-order) resonance with a perturbing force with frequency Ω_R . In this case, the standard expression for the phase of the streamlines is (Shu 1984):

$$\phi = |m|(\lambda - \Omega_R t) + \frac{3(m-1)M_P}{4\pi\sigma_0 a_L^4} (a - a_L)^2, \quad (26)$$

where a_L is the semimajor axis of the exact resonance. Note that the sign on the second term ensures that the phase increases with increasing a for waves with $m > 1$ and $m < 0$. In the $m > 1$ case, the wave only exists exterior to a_L and so increasing a corresponds to increasing $(a - a_L)^2$, while in the $m < 0$ case the wave only exists interior to a_L so increasing a corresponds to decreasing $(a - a_L)^2$. Combining Equations (26) and (16) yields the correct pattern speed

$$\Omega_p = \Omega_R. \quad (27)$$

Furthermore, combining Equations (26) and (15) yields the standard expression for the wavenumber as a function of distance from the resonance:

$$k(a, t) \simeq \frac{3}{2} |m-1| \frac{M_P}{\pi\sigma_0 a_L^4} |a - a_L|. \quad (28)$$

However, it is now useful to rewrite this expression in a slightly different form:

$$k(a, t) \simeq \left(\frac{3}{2} |m-1| \sqrt{\frac{GM_P}{a_L^5}} \right) \times \frac{\sqrt{GM_P/a_L^3}}{\pi G\sigma_0} |a - a_L|, \quad (29)$$

where the term in brackets is the same as dk/dt for the freely evolving spiral pattern. This means the second term should have units of time, and indeed it is the time it would take a spiral wave-like disturbance to propagate the distance between a and a_L .

To see why this is indeed the case, recall that the dispersion relation for density waves in a ring has the form (Shu 1984; see Equation (24) above)

$$(\omega - mn)^2 = \kappa^2 - 2\pi G\sigma_0 |k|, \quad (30)$$

where $\omega = |m\Omega_p|$ is the (positive-definite) frequency of the pattern at a fixed radius and longitude. Thus, we obtain the following standard expression for the group velocity:

$$v_g = \frac{\partial\omega}{\partial k} = \frac{-\pi G\sigma_0}{(\omega - mn)} = \text{sign}(m) \frac{\pi G\sigma_0}{\kappa}, \quad (31)$$

where in the last expression we assume that $\Omega_p = n - \kappa/m$, which is a good approximation for all density waves. Furthermore, if we assume $\kappa \simeq \sqrt{GM_P/a^3}$, then we find the group velocity of the wave is given by the standard expression:

$$v_g \simeq \text{sign}(m) \frac{\pi G\sigma_0}{\sqrt{GM_P/a^3}}. \quad (32)$$

Note that this expression is independent of wavenumber, which means that if the surface mass density remains constant, a wave will propagate at a constant speed regardless of what its wavelength currently is or how its wavelength has evolved over time. Furthermore, this means that Equation (29) can be written as

$$k(a, t) \simeq \left(\frac{3}{2} |m - 1| \sqrt{\frac{GM_P}{a_L^5}} \right) \frac{|a - a_L|}{|v_g|}, \quad (33)$$

or, equivalently,

$$k(a, t) \simeq \frac{3}{2} |m - 1| \sqrt{\frac{GM_P}{a_L^5}} \delta t, \quad (34)$$

where δt is the time a wave fragment would have taken to travel the distance $a - a_L$. Note that since $a - a_L$ and v_g have the same sign, we can also say $\delta t = (a - a_L)/v_g$.

The observed wavelengths for both freely winding patterns and resonantly driven waves can therefore be understood in the same basic framework. That is, the wavenumbers of both these structures increase linearly with time at a set rate, and the observed trends with distance at a given time arise either because this rate varies with position (for free spiral patterns) or because the wave travels progressively further away from where it was originally excited (for resonantly driven density waves).

3.1.4. Detached Density Wave Fragments

Finally, let us consider the case where a wave fragment is launched from one location and propagates through the ring. We will assume here that part of a wave is created by a resonance at semimajor axis a_L with a fixed pattern speed, but at some time the resonant forcing stops and the wave continues to propagate through the ring at the speed v_g and with a pattern speed Ω_p equal to the local free streamline rotation rate $\Omega_s = n(a) - \kappa(a)/m$. (Note that while this is again not precisely true for the observed density waves, the differences between Ω_p for the observed waves and Ω_s are of order 1–2 parts in 10^4 , and so can be neglected for these particular calculations.)

Let us define the time when the resonant forcing stops as $t = 0$. At that time, we have a standard forced density wave, and so the wave phase is given by Equation (26), and the corresponding value of ϕ_0 is

$$\phi_0(a = a_i, t = 0) = -\frac{3(m-1)M_P}{2|m|\pi\sigma_0 a_L^4} \frac{1}{2} (a_i - a_L)^2. \quad (35)$$

Note that we designate the semimajor axis of the wave at this particular time as a_i in order to distinguish this from its observed location at a time δt_o after the resonant forcing stops. We will designate the observed location of this part of the wave at that time as a_o . If we assume a constant group velocity v_g , these two quantities are related by the expression $a_o = a_i + v_g \delta t_o$. Of course, in reality, the group velocity does vary with semimajor axis (see Equation (32)), but since the wave travels a small fraction of its original semimajor axis (less than 100 out of 80,000 km), these variations in v_g should be less than 1%, which can be neglected here. Furthermore, if we assume that v_g can be approximated as a constant, we can rewrite the above expression for the initial phase in the following way:

$$\phi_0(a = a_i, t = 0) = -\frac{3(m-1)}{2m} \sqrt{\frac{GM_P}{a_L^5}} \frac{1}{2} v_g \delta t_i^2, \quad (36)$$

where $\delta t_i = (a_i - a_L)/v_g$ is an estimate of how much time has elapsed since the relevant part of the wave was formed at the resonance. Note that this quantity is always positive, since v_g and $a_i - a_L$ always have the same sign.

After $t = 0$, the wave not only propagates a finite distance through the rings, but it also accumulates an additional phase shift, given by the following expression:

$$\begin{aligned} \delta\phi_0 &= \phi_0(a = a_o, t = \delta t_o) - \phi_0(a = a_i, t = 0) \\ &= \int_0^{\delta t_o} \Omega_s(a(t')) dt' = \int_0^{\delta t_o} \Omega_s(a_i + v_g t') dt' \end{aligned} \quad (37)$$

which we may evaluate by expanding to first order in $v_g t'$:

$$\delta\phi_0 = \int_0^{\delta t_o} \left(\Omega_s(a_i) + v_g t' \frac{\partial\Omega_s}{\partial a} \Big|_{a=a_i} \right) dt' \quad (38)$$

and then doing the integrals:

$$\delta\phi_0 = \Omega_s(a_i) \delta t_o + \frac{1}{2} v_g \delta t_o^2 \frac{\partial\Omega_s}{\partial a} \Big|_{a=a_i}; \quad (39)$$

or, equivalently:

$$\delta\phi_0 = \Omega_s(a_i) \delta t_o - \frac{3(m-1)}{2m} \sqrt{\frac{GM_P}{a_i^5}} \frac{1}{2} v_g \delta t_o^2. \quad (40)$$

Note that this phase shift only depends explicitly on a_i , not $a_o = a_i + v_g \delta t_o$. If we take the time derivative of this expression, assuming a_i is independent of time, then we get the correct local pattern speed at a_o :

$$\begin{aligned} \Omega_p &= \frac{\partial\delta\phi_0}{\partial\delta t_o} \Big|_{a_i} = \Omega_s(a_i) + v_g \delta t_o \frac{\partial\Omega_s}{\partial a} \Big|_{a=a_i} \\ &= \Omega_s(a_i + v_g \delta t_o) = \Omega_s(a_o). \end{aligned} \quad (41)$$

If we want to reexpress this in terms of a_o , we need to be careful, because if we replace a_i with simply $a_o - v_g \delta t_o$, then the phase shift can be rewritten in the following form (to first order in $v_g \delta t_o$):

$$\delta\phi_0 = \Omega_s(a_o) \delta t_o - \frac{1}{2} v_g \delta t_o^2 \frac{\partial\Omega_s}{\partial a} \Big|_{a=a_o}. \quad (42)$$

However, in this case the pattern speed becomes:

$$\begin{aligned}\Omega_p &= \left. \frac{\partial \delta \phi_0}{\partial \delta t_o} \right|_{a_o} = \Omega_s(a_o) - v_g \delta t_o \left. \frac{\partial \Omega_s}{\partial a} \right|_{a=a_o} \\ &= \Omega_s(a_o - v_g \delta t_o) = \Omega_s(a_i),\end{aligned}\quad (43)$$

which would mean the speed of the pattern does not change as it propagates, contradicting our original assumption. The issue is that a fixed a_i only corresponds to a fixed a_o at one particular value of time, so the correct relationship is $a_i = a_o - v_g \tau_o$, where τ_o is a fixed number that equals δt_o at the time of the observation. In this case, we obtain the following expression for $\delta \phi_0$:

$$\delta \phi_0 = \Omega_s(a_o) \delta t_o - v_g \tau_o \left. \frac{\partial \Omega_s}{\partial a} \right|_{a=a_o} + \frac{1}{2} v_g \delta t_o^2 \left. \frac{\partial \Omega_s}{\partial a} \right|_{a=a_i}. \quad (44)$$

This yields the following expression for the pattern speed:

$$\left. \frac{\partial \delta \phi_0}{\partial \delta t_o} \right|_{a_o} = \Omega_s(a_o) - v_g \tau_o \left. \frac{\partial \Omega_s}{\partial a} \right|_{a=a_o} + v_g \delta t_o \left. \frac{\partial \Omega_s}{\partial a} \right|_{a=a_i}, \quad (45)$$

where the last two terms cancel out to first order at the time when $\tau_o = \delta t_o$, leaving the desired value of Ω_s at the observed location. In order to get the wavenumber, we need to compute the absolute phase of the wave by adding Equations (40) and (36). If we choose to leave things in terms of a_i , then we can note that one term in Equation (40) has a very similar form to the initial phase in Equation (36), except that δt_o replaces δt_i and a_i replaces a_L . Since $a_i - a_L \ll a_L$, we can approximate a_i as a_L in this expression, and then combine this with Equation (36) to get the following expression for the phase:

$$\begin{aligned}\phi_0(a_o, \delta t_o) &= \Omega_s(a_i) \delta t_o \\ &- \frac{3(m-1)}{2m} \sqrt{\frac{GM_P}{a_L^5}} \left(\frac{1}{2} v_g \delta t_o^2 + \frac{1}{2} v_g \delta t_i^2 \right).\end{aligned}\quad (46)$$

We can now convert this into an explicit function of a_o by again using the identity $a_i = a_o - v_g \tau_o$, which yields:

$$\begin{aligned}\phi_0(a_o, \delta t_o) &= \Omega_s(a_o - v_g \tau_o) \delta t_o \\ &- \frac{3(m-1)}{2m} \sqrt{\frac{GM_P}{a_L^5}} \\ &\times \left(\frac{1}{2} v_g \delta t_o^2 + \frac{1}{2} \frac{(a_o - v_g \tau_o - a_L)^2}{v_g} \right),\end{aligned}\quad (47)$$

where we have also used the identity $\delta t_i = (a_i - a_L)/v_g$. Note that when we take the derivative to get the wavenumber, we assume that δt_o is a constant, and so we can just equate $\tau_o = \delta t_o$. Taking the appropriate derivative to get the radial wavenumber then yields:

$$\begin{aligned}k(a_o, t) &= -|m| \left. \frac{\partial \Omega_s}{\partial a} \right|_{a=a_i} \delta t_o \\ &+ \frac{3(m-1)}{2m} \sqrt{\frac{GM_P}{a_L^5}} \frac{(a_o - v_g \delta t_o - a_L)}{v_g}.\end{aligned}\quad (48)$$

Rewriting the second term back in terms of $\delta t_i = (a_i - a_L)/v_g$, substituting in the above expression for $\partial \Omega_s / \partial a$ and again

assuming $a_i \simeq a_L$, this becomes:

$$k(a_o, t) = \frac{3}{2} |m-1| \sqrt{\frac{GM_P}{a_L^5}} (\delta t_o + \delta t_i). \quad (49)$$

This is the sensible generalization of the previous expressions, demonstrating that even in this case the wavenumber at a given location is proportional to the time elapsed since the wave was generated (which is $\delta t_o + \delta t_i$ here).

3.1.5. Model Summary

Since all these different cases yield the same basic expression for k , we can use the observed wavenumber and location of any wave to deduce when the wave was formed and its original pattern speed. First of all, given the observed k of a wave with a specified m at a given radius r , the elapsed time since that particular part of the wave formed is given by the following expression:

$$\delta t = \frac{2k}{3|m-1|} \sqrt{\frac{r^5}{GM_P}}. \quad (50)$$

Furthermore, given this time and an estimate of the surface mass density σ_o , we can estimate the radial displacement experienced by the wave to be:

$$\delta r = v_g \delta t \simeq \text{sign}(m) \frac{2\pi k \sigma_o r^4}{3|m-1|M_P}, \quad (51)$$

which can be used to deduce the wave's initial location. The corresponding initial pattern speed can also be estimated using Equation (17).

The above expressions do rely on a couple of approximations that are worth keeping in mind. First of all, we assume that $r = a = a_L$ here, which is a good approximation for any sensible density wave, since $a - a_L \ll a$ and the mean radius of any low-eccentricity orbit should be close to a . We also neglect the small deviations between Ω_s given by Equation (17) and the true pattern speed of the wave, which should only affect these calculations by a fraction of a percent in the C ring. More importantly, we here assume $n \simeq \kappa \simeq \sqrt{GM_P/a^3}$. The difference between n and κ in Saturn's rings is only 0.5%–2%, so this approximation is reasonably good for all of the waves considered here. However, if one wants to use this method to obtain estimates of the pattern speeds at higher precision than a few percent of the wave's total displacement, then they will need to use more complex expressions for the pattern winding rates, which may differ between free waves and resonantly driven waves. Such complications are well beyond the scope of this particular analysis.

3.2. Validation of the Phenomenological Model

In order to validate the above model, we can consider waves generated by the co-orbital moons Janus and Epimetheus. Every four years, mutual gravitational interactions between these moons causes each of them to swap between two different semimajor axes, producing distinct changes in their mean motions that change the locations of their mean motion resonances in the rings. Prior studies by Tiscareno et al. (2006) showed that the unusual morphologies of the density waves generated at these locations could be modeled as a series of wave fragments generated by the moons at different times.

This is the same basic idea behind the model described above, and since the orbital history of these moons is well established, these waves provide a useful test case.

More specifically, let us consider the wave associated with the 7:5 resonances with Janus and Epimetheus. This wave occurs in the outer Cassini Division, where the surface mass density is around 10 g cm^{-2} , which is closer to typical conditions in the C ring than other Janus waves found in the A and B rings. We will also use wave profiles derived from the same three occultations used in Section 2.1 to illustrate the time evolution of the C ring structures. The top left panel of Figure 11 shows these three occultation profiles. Note that the location of the wave signal differs among the three profiles, due to the changing locations of the two moons. The most prominent wave signals in all of these profiles are due to the larger moon Janus, but weak wave signals can be seen around 121,250 km in the first and last occultation, which are likely due to the smaller moon Epimetheus.

The three other panels on the left of Figure 11 show wavelet transforms of these three profiles, which show the strength of the periodic signals as functions of radius and wavenumber. For normal density waves, these wavelets would show a diagonal band, but in these cases the pattern is more complicated. In particular, for the first and last occultation, the band shows a distinct kink around wavenumbers of 2 km^{-1} , while for the middle observation, the signal seems to disappear around the same wavenumber. These anomalies can be attributed to the periodic changes in the moons' orbits, and this connection can be dramatically confirmed by using Equation (50) to convert the wavenumber values into estimates of when the patterns were generated (shown on the right-hand axes of each plot), and marking the times when the moon's orbits changed near the start of 1998, 2002, 2006, 2010, and 2014. The sudden changes in the strength or slope of the dominant signals fall close to those times, as one would expect. Furthermore, if we take a closer look at these wavelets, we can see in both the RCas 106i and gamCru245e occultations that there is a signal around 121,250 km that is only clearly present in the time ranges of 2002–2006 and 2010–2014. This signal is absent from the gamCru187i observation, but another signal can be seen around 121,300 km between 2006 and 2010. This signal is consistent with the shifting signals from Epimetheus.

We can further confirm the associations between these signals and the changing motions of the moons if we account for the radial propagation of the wavelet signals by shifting the wavelet signal at each wavenumber by the amount given in Equation (51). This shift depends on the assumed surface mass density, which for this wave we will assume to be 11 g cm^{-2} , consistent with the values derived from nearby waves (Colwell et al. 2009). These corrected wavelet transforms are shown in the lower three panels on the right of Figure 11. In this case, the horizontal axis is no longer the observed radius, but is instead the inferred radius where the wave patterns originated from at the indicated date. In these panels, we not only plot horizontal lines corresponding to the dates of the orbital swaps, but we also provide vertical lines marking the nominal positions of the resonances with the moons at different times. Note that the location of the Janus resonance oscillated between the two locations around 121,250 km, while the Epimetheus resonances oscillated between the locations around 121,220 and 121,280 km, respectively. In these plots, we see that during the times between 2002–2006 for RCas106i, 2006–2010 for

gamCru187i, and 2010–2014 for gamCru245e, the two signals are aligned with the expected locations of the signals from Janus and Epimetheus. Furthermore, prior to these epochs, the strong Janus signal moves in the appropriate direction in all three cases.⁶

For the RCas106i and gamCru245e signals, the trends in the data before the shift are not particularly well aligned with the expected signals, but this can be explained as a result of the finite wavelength resolution of the wavelet transform. Around 121,300 km in both profiles is the location where both components of the wave are overlapping, and the finite wavenumber sensitivity of the transform is blurring the two signals together into a nearly vertical band in the raw wavelet, which is then sheared in the transformed wavelet. Note that for the gamCru187i data this is less of an issue, since the signal created before 2006 shifts outward, away from the more recent wave, and so shows the expected trend. The patch shifting inward in this case is instead due to a small data gap in the profile, coupled with the overprinted Epimetheus wave. These panels therefore show that these transformed wavelets can document variations in the ring perturbations over time, but also reveal that these reconstructions may be imperfect if there are multiple overprinted patterns at the same radius.

Finally, the top right panel of Figure 11 shows the average signal amplitude between two swaps from each of the wavelet transforms below. These plots are all normalized so that the peak of the Janus signal is unity, and all three show that the signal from the Epimetheus resonance is between 0.4 and 0.5 times the signal from Janus. This is perfectly consistent with the expected perturbations from the two moons. The mass ratio of the two moons is 0.278 (Jacobson et al. 2008), but these particular resonances are second order, and so the perturbations are proportional to the product of the moon's mass and orbital eccentricity (Tiscareno & Harris 2018). Janus's eccentricity is 0.0068, while Epimetheus's is 0.0097 (Jacobson et al. 2008), so the expected ratio of the perturbation strengths is 0.4, which is consistent with these curves. This implies that the wavelet amplitude at each wavenumber is a good measure of the different perturbations' relative strengths.

3.3. Procedures for Extracting the History of Planetary Asymmetries

Having established a theoretical framework for interpreting waves generated by time-variable periodic forces, we can now discuss the analytical methods for translating the observed ring structures into a historical record of asymmetries in the planet's gravitational field. These techniques start with the average phase-corrected power \mathcal{P}_ϕ and power ratio \mathcal{R} for the three sets of occultations given in Table 1, assuming $m = 3$ or $m = -1$. The ratio \mathcal{R} yields higher signal-to-noise detections of the relevant wave signals, while \mathcal{P}_ϕ enables the relative amplitudes of the strongest wave signals to be quantified. For this particular analysis, both these quantities are computed using wavelet transforms of the residual normal optical depth profiles $\tau_r = \tau_n - \bar{\tau}_n$, where $\bar{\tau}_n$ is the average normal optical depth across all of the occultations. Subtracting $\bar{\tau}_n$ has little effect on the wave signals in each profile, but has the advantage of removing the sharp edges that bound the various plateaux from

⁶ Note that the wave signals are weak for wavenumbers below 1 km^{-1} because the wave amplitude initially grows linearly with distance from the resonance (see Section 3.3.3). This causes the signal amplitudes to be low for a time period within a few years of the observation.

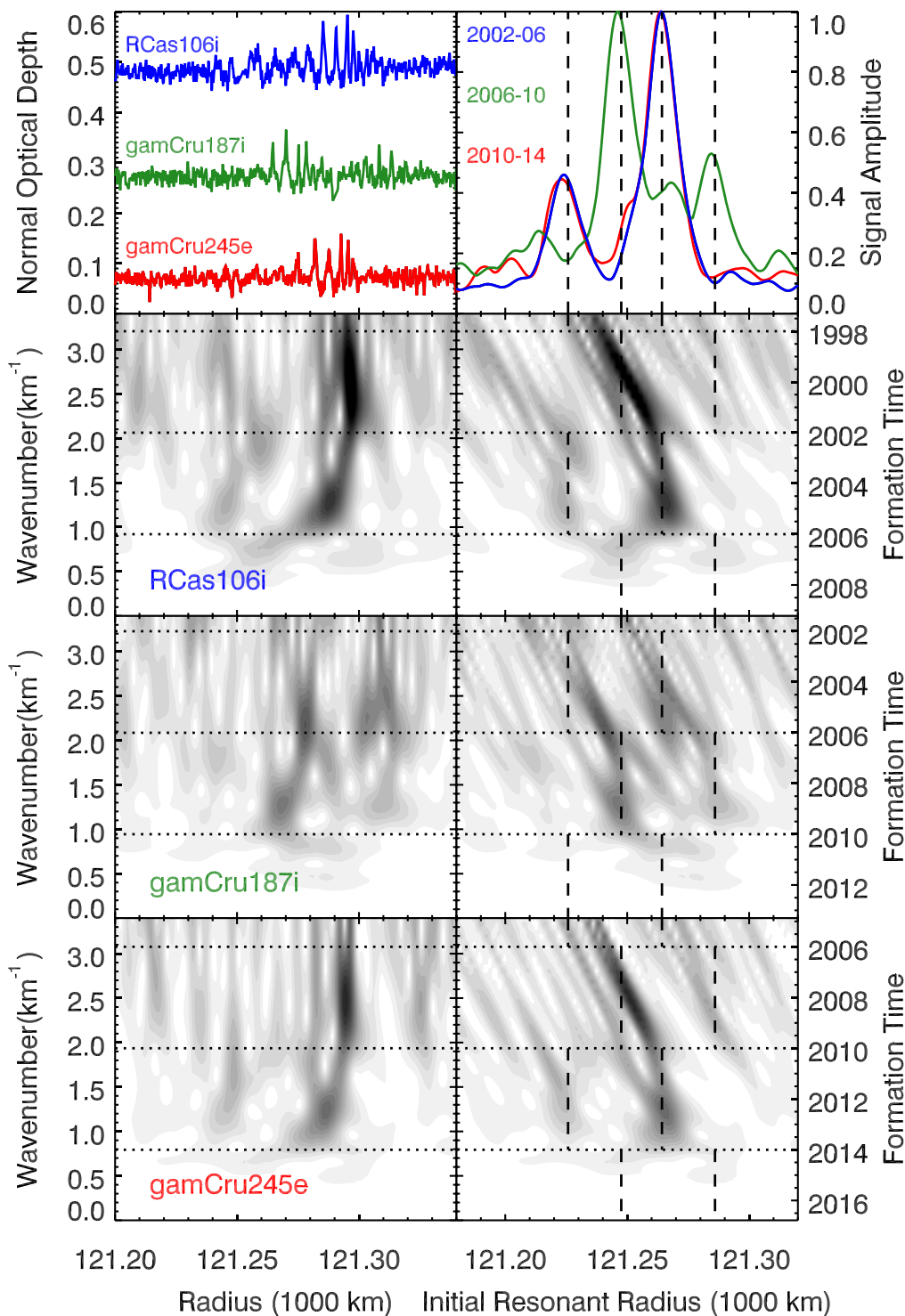


Figure 11. An example of using wavelet transforms to document recent ring history. The top left panel of this image shows three profiles of the density wave generated in the Cassini Division by the 7:5 resonances with Janus and Epimetheus. Note that the structure of this wave changes over time due to the moons’ orbital swaps every four years. The bottom three panels on the left show wavelet transforms of these three profiles, giving the strength of the periodic signals as functions of radius and wavenumber. Overlaid on these plots are horizontal lines corresponding to the times when the moons undergo an orbital swap. Note the changes in the slopes and locations of the wave signals at these times. The lower right three panels show wavelet transforms that have been adjusted to remove the outward propagation of the wave patterns, assuming a surface mass density of 11 g cm^{-2} . These plots also include overlaid vertical lines marking the positions of the resonances with the two moons as functions of time. The top right panel shows the normalized average signal strength in the indicated time range for each of the below transforms, showing the consistent relative strength of the signals from the two moons.

all of the profiles. These edges produce wavelet signals over a broad range of wavenumbers, and while these signals are reduced when the phase-corrected signals are averaged together to give \mathcal{P}_ϕ , they are not completely eliminated due to the finite

number of occultations in each set. Using τ_r profiles therefore yields much cleaner maps of the desired signals.

Since the structures of interest here have a range of pattern speeds, we actually compute \mathcal{R} and \mathcal{P}_ϕ at each radius for a

range of pattern speeds around the expected local rate Ω_p given by Equation (17), corresponding to a span of ± 200 km in resonant radius. We then find the maximum values of both of these parameters at each radius and wavenumber for resonant radii within 90 km of the observed location, which we will designate as \mathcal{R}^{\max} and \mathcal{P}_ϕ^{\max} . We also estimate the wavelet amplitude due to the optical depth variations associated with the relevant waves as a function of radius and wavenumber as:

$$A_w = \frac{\mathcal{N}}{\bar{\tau}_n} \sqrt{\mathcal{P}_\phi^{\max}}, \quad (52)$$

where \mathcal{N} is the standard normalization factor that depends on the radial resolution of the profiles δr_{res} , as well as the wavenumber k and its sampling frequency δk_{res} (Torrence & Compo 1998):

$$\mathcal{N} = \frac{\sqrt{\delta r_{\text{res}} \delta k_{\text{res}}}}{k^{1/2}}. \quad (53)$$

Note that we designate this wavelet amplitude A_w to distinguish it from the amplitude of the variations in the optical depth profile $A(r)$.

In order to translate the observed signals in \mathcal{R}^{\max} and A_w as a function of observed radius r_o and wavenumber k into estimates of the properties and strengths of the gravitational asymmetries as a function of rotation rate and time, we need to perform the following three operations:

1. Convert the observed wavenumbers into estimates of the wave initiation time using Equation (50).
2. Translate the radial locations of the features into the original resonance location and perturbation pattern speed/rotation rate using Equations (51) and (17).
3. Convert the observed wave amplitudes into estimates of the perturbations in the gravitational potential based on the observed amplitudes of comparable satellite-generated density waves.

Each of these steps is discussed in detail below.

3.3.1. Converting Wavenumbers to Wave Initiation Times

Converting the observed wavenumbers to wave initiation times is the most straightforward step in this process because Equation (50) allows wavenumbers to be directly translated into the time that has elapsed since the wave was formed. We can then convert these elapsed times into absolute times by adding back the mean dates for each set of occultations, which are 2008.8, 2013.5, and 2017.2 for the three epochs in Table 1. This enables us to express both \mathcal{R}^{\max} and A_w as functions of the observed radius and wave initiation time t_i .

3.3.2. Translating Radial Locations to Rotation Rates of Original Perturbations

Translating the radial locations of the structures into the rotation rate of the original perturbation is a more involved process because it needs to account for the fact that any wave with a finite wavenumber has propagated a finite distance. Furthermore, the distance the wave propagates depends on the ring's surface mass density, which can vary on a variety of spatial scales. Fortunately, the theoretical framework provided in Section 3.1 above provides a novel way to estimate the

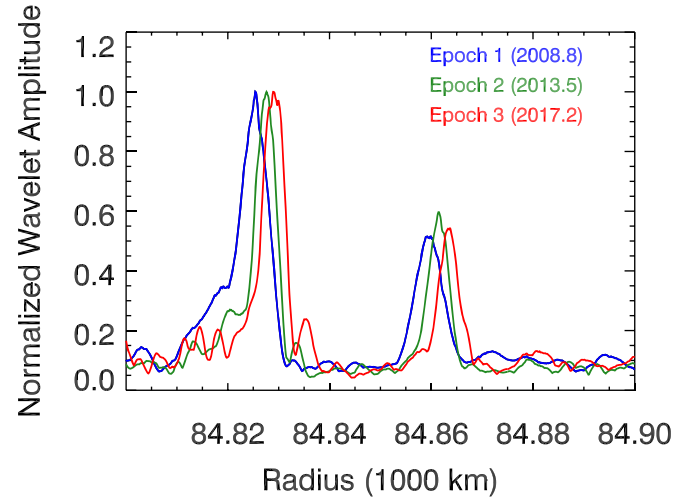


Figure 12. Plots of the normalized wavelet amplitudes A_w for waves generated in the year 2000 as a function of the observed position at the three observation epochs. Note that since all three profiles correspond to a fixed absolute initiation time, each profile is for a different wavenumber value in the wavelet. The signal peaks move to larger radii over time, consistent with the trends observed in Figure 1.

group velocity and surface mass density, by comparing observations made at different times.

The basic idea is that given arrays of A_w values⁷ derived from observations at different times, we can choose a wavenumber for each array that corresponds to one particular wave initiation time and generate profiles of wave signal strength versus radius that contain peaks at locations corresponding to waves generated at that specific time. Figure 12 shows an example of the amplitude profiles for wave signals generated in the year 2000 derived from the three different observation epochs. Each of these profiles shows two peaks that correspond to the waves seen in Figure 1, but the locations of these peaks shift to larger radii for observations taken at later times, because of how the wave propagated through the rings. More quantitatively, the difference in the wave signal's position between two profiles is $\Delta r = v_g \Delta t$, where Δt is the time elapsed between the two observations and v_g is the group velocity given by Equation (32). We can therefore use the observed radius shift between the peaks Δr and the known time between the observations Δt to estimate v_g as just $\Delta r / \Delta t$. Furthermore, we can solve Equation (32) to obtain the following estimate for the local unperturbed surface mass density:

$$\sigma_o = \frac{\kappa \Delta r}{\pi G \Delta t}. \quad (54)$$

In practice, we estimate Δr as the offset that yields the maximum cross-correlation coefficient between a pair of profiles covering a specified radius range that includes wave signals. For each radial range and each pair of A_w arrays, we estimate Δr for signals initiated each year between 1980 and 2005. We then select out the Δr estimates for which the peak correlation coefficient is higher than some threshold value (either 0.5 or 0.75), and take the mean and standard deviation of those data to derive estimates and uncertainties for the surface mass density. Table 2 and Figure 13 summarize the results of these calculations. Note that the estimated uncertainties

⁷ We also considered the \mathcal{R}^{\max} arrays, but they were not as suitable for this because of signal-to-noise considerations.

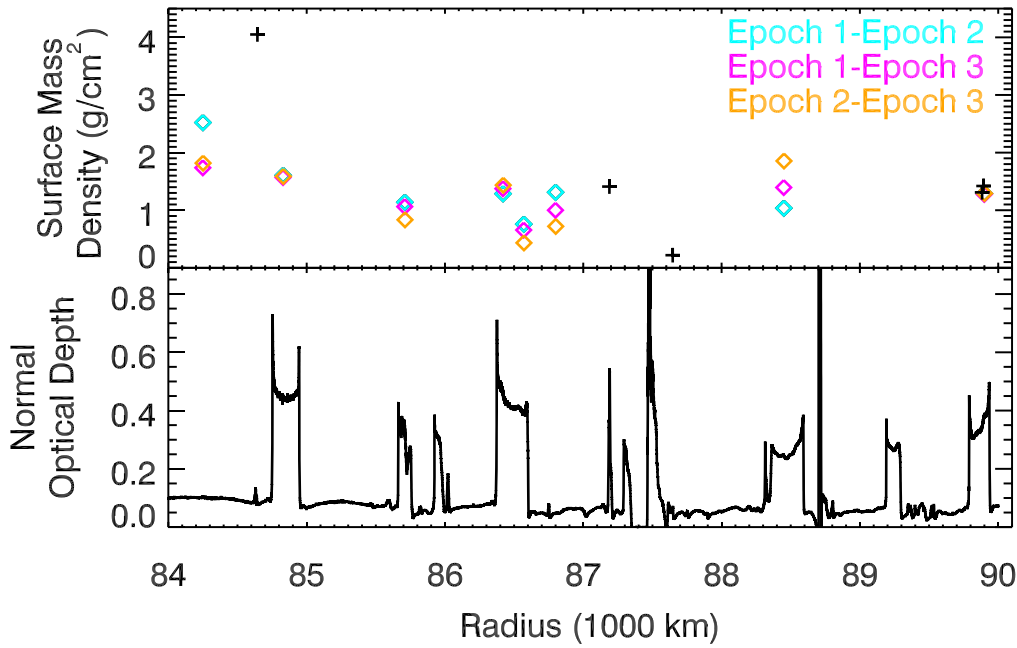


Figure 13. Estimates of the ring’s surface mass density derived from the observed group velocities of the waves. The colored diamonds are the results of this analysis, while the plus signs are based on standard density wave analyses (Baillié et al. 2011; Hedman & Nicholson 2013).

Table 2
Mass Density Estimates Derived from Group Velocity Estimates for the $m = 3$ and $m = -1$ Waves in the C Ring

Radius Range (km)	Assumed m	Cross-Corr. Limit	Mass Density (g cm^{-2})		Mass Density (g cm^{-2})		Mass Density (g cm^{-2}) Combined
			Epoch 1–Epoch 2	Epoch 1–Epoch 3	Epoch 2–Epoch 3	Epoch 2–Epoch 3	
84200–84300	3	0.5	2.52 ± 0.82	1.74 ± 0.86	1.82 ± 0.76	2.02 ± 0.43	
84780–84880	3	0.75	1.61 ± 0.08	1.57 ± 0.04	1.59 ± 0.06	1.59 ± 0.02	
85660–85760	-1	0.75	1.14 ± 0.03	1.06 ± 0.03	0.83 ± 0.03	1.01 ± 0.16	
86370–86470	3	0.75	1.29 ± 0.04	1.37 ± 0.03	1.44 ± 0.04	1.37 ± 0.08	
86520–86620	3	0.75	0.76 ± 0.09	0.66 ± 0.07	0.43 ± 0.06	0.62 ± 0.16	
86750–86850	3	0.5	1.31 ± 0.23	1.00 ± 0.24	0.72 ± 0.03	1.01 ± 0.29	
88400–88500 ^a	3	0.5	1.04 ± 0.06	1.39 ± 0.03	1.86 ± 0.08	1.42 ± 0.41	
89850–89950 ^b	3	0.75	1.29 ± 0.03	1.28 ± 0.02	1.29 ± 0.02	1.28 ± 0.01	

Notes. Note that error estimates for each pair of epochs are based on the scatter among the different initiation time slices, while the error on the combined estimate is based only on the scatter among the three different epoch pairs.

^a The region containing the Prometheus 4:2 density wave.

^b The region containing the Pandora 4:2 and Mimas 6:2 density waves.

from each pair of epochs are often smaller than the scatter among the measurements. This most likely reflects finite correlations between the signal profiles at different years due to the finite wavelength resolution of the wavelet transform. Rather than explicitly computing these correlations, we instead just consider the scatter among the mass density estimates from the different pairs of epochs as being more representative of the real uncertainty.

We can validate this method of estimating surface densities by first considering the density estimate for the region between 89,850 and 89,950 km, which covers the locations of the Mimas 6:2 and Pandora 4:2 density waves. Baillié et al. (2011) estimated the ring surface mass density based on the radial wavelength trends in these waves as 1.33 ± 0.20 and $1.42 \pm 0.21 \text{ g cm}^{-2}$, respectively, which are in very good agreement with our estimate of around 1.28 g cm^{-2} . This indicates that this approach to measuring surface mass densities works well, at least for satellite waves. Further reinforcing this view is that when we apply this technique to the region

between 88,400 and 88,500 km, a region of similar optical depth that should contain the Prometheus 4:2 wave, we obtain similar estimates of the surface mass density, albeit with larger uncertainties.

Turning to the waves generated by the planet between 84,000 and 87,000 km, we continue to find reasonably consistent results at most locations. For the regions 84,780–84,880 and 86,370–86,470 km, which correspond to the strongest $m = 3$ waves, we get fairly consistent estimates of the surface mass density. The dispersion among the estimates is somewhat larger for some of the other regions containing $m = 3$ waves and the region containing the $m = -1$ waves, but all of the measurements between 84,500 and 87,000 km fall in a range between about 0.6 and 1.6 g cm^{-2} , which is compatible with the value of 1.41 g cm^{-2} derived from an analysis of the nearby wave W87.19 (Hedman & Nicholson 2013). Note that these mass densities are smaller than the prior estimates derived by Hedman & Nicholson (2014) under the mistaken assumption that these waves did not evolve over time. The consistency of these

numbers provides further evidence that this approach yields sensible estimates of the surface mass density.

One possible inconsistency is that prior analyses of the wave W84.64, identified as an $m = -2$ saturnian normal mode by Hedman & Nicholson (2013), indicated a mass density of 4.05 g cm^{-2} around that wave, a factor of 2 higher than any of the estimates obtained here, even including those that occur quite close to that wave. Furthermore, there is a weak $m = 3$ wave interior to W84.64 around 84,250 km, and an analysis of this region yields mass densities between 2 and 3 g cm^{-2} (albeit with a fair amount of scatter). It is therefore not clear whether there is a sharp edge or peak in the surface mass density around 84,500 km that is not obvious in the optical depth, or if there is some error in the prior calculation of the surface mass density from W84.64. Such details are best left to future work.

For a given value of σ_o , we can translate the observed radius of a feature r observed at a time t_o to the location where the wave originated from r_i using the formula $r_i = r_o - v_g(t_o - t_i)$, where t_i is the wave initiation time given in the previous subsection. Applying this transformation to all wave initiation times yields the arrays $\mathcal{R}^{\max}(r_i, t_i)$ and $A_w(r_i, t_i)$, or, equivalently, $\mathcal{R}^{\max}(\Omega_p, t_i)$ and $A_w(\Omega_p, t_i)$, where Ω_p is the resonant pattern speed at each r_i given by Equation (17). In principle, we could analyze each wave fragment using the best-fit surface mass densities at each location. However, in practice, the observed variations in the surface mass density are small enough to be ignored for the purposes of this initial study, and so for the sake of simplicity we will simply assume a uniform surface mass density of 1.3 g cm^{-2} for this entire region. Note that the errors in r_i and Ω_p induced by an incorrect estimate for σ_o grow linearly with the age of the wave fragment, but even after 30 yr (the time frame we can currently probe) an error of $\pm 0.5 \text{ g cm}^{-2}$ in σ_o will only produce errors in r_i of around 7 km, which corresponds to errors in Ω_p of order 0.1 day^{-1} , assuming an $m = 3$ wave and 0.3 day^{-1} for an $m = -1$ wave.

3.3.3. Converting Wave Amplitudes to Perturbation Potential Amplitudes

While the array $\mathcal{R}^{\max}(\Omega_p, t_i)$ already provides a direct estimate of the signal-to-noise ratio for any wave fragments, we still need to convert the wavelet amplitudes A_w into estimates of the gravitational potential perturbations Φ'_m responsible for making these waves. Such conversions are nontrivial, because as a wave fragment propagates through the rings, its amplitude evolves in response to two competing processes. At first, the wave's amplitude increases over time as the wavenumber increases due to decreasing distances between ring particle streamlines. Eventually, however, dissipation due to collisions among ring particles causes the amplitude of the pattern to fall back toward zero (Shu 1984; Tiscareno et al. 2007). Hence, the amplitude of the gravitational perturbation required to produce a wave fragment of a given amplitude depends on the age (or wavenumber) of that fragment.

In principle, one could use theoretical models to translate the observed A_w at a given wavenumber into estimates of Φ'_m . However, in practice, such an approach is not yet viable. First of all, a density wave's amplitude not only depends on the gravitational perturbation, but also on the local surface mass density, the effective kinematic viscosity of the ring material, and the azimuthal wavenumber m (Shu 1984; Nicholson et al. 1990; Tiscareno et al. 2007; Tiscareno & Harris 2018). Second, the wavelet amplitude A_w is not the same thing as the actual

amplitude of the wave in the profile, both because a wavelet transform disperses the signal from the wave over a range of wavenumbers (Torrence & Compo 1998) and because the finite spatial resolution of the profile has wavelength-dependent effects on the measured wave amplitude. A general method that can account for all of these different phenomena is well beyond the scope of this investigation.

Instead, we employ an empirical approach that uses nearby satellite waves to determine the relevant conversion factors. There are three $m = 3$ waves situated within the C ring plateaux generated by the Mimas 6:2, Pandora 4:2, and Prometheus 4:2 resonances. These three waves are not only found in environments similar to the majority of the time-variable $m = 3$ and $m = -1$ signals, but they also have the same value of $|m - 1|$ as all of those waves. The conversion factors between A_w and Φ'_m for these three satellite waves should therefore be most similar to those of the relevant planet-generated waves (see the Appendix for details). Furthermore, the Φ'_m values for each of the satellite waves can be explicitly calculated (see the Appendix), so these conversion factors can be derived from the measured wavelet signals. We therefore determine the peak wavelet signal associated with each of these waves at each epoch and wave initiation time by finding the maximum value of $A_w(\Omega_p, t_i)$ within a selected range of pattern speeds surrounding the expected location of the desired wave ($762.5\text{--}763.5 \text{ day}^{-1}$ for the Mimas 6:2 wave, $762.5\text{--}762.95 \text{ day}^{-1}$ ⁸ for the Pandora 4:2 wave, and $781.5\text{--}782.5 \text{ day}^{-1}$ for the Prometheus 4:2 wave). Figure 14 shows the resulting profiles of peak wavelet amplitude versus elapsed time. All of these profiles show a clear amplitude peak between 15 and 30 yr, which is roughly consistent with the dimensionless damping lengths of around 6.65 found by Baillié et al. (2011), which would correspond to a characteristic damping time of around 22 yr (see the Appendix).

The Mimas 6:2 wave has both the largest amplitude and the smallest dispersion among the data from the different epochs, so we choose to use that wave alone to estimate the conversion factors from A_w to Φ'_m , with the other two waves being used to check the validity of those conversions. The gravitational potential perturbation associated with the Mimas 6:2 wave is a constant value of $33 \text{ cm}^2 \text{ s}^{-2}$ (Tiscareno & Harris 2018; see also the Appendix), and we can estimate the peak amplitude of the Mimas 6:2 wave as a function of elapsed time δt as the average of the three curves derived from the three epochs shown in Figure 14 (this average is shown as the black curve in the top panel of that figure, as well as in Table 3). We can therefore estimate the perturbation potential responsible for the wavelet signals by simply dividing each column of an $A_w(\Omega_p, t_i)$ array by this normalization curve and then multiplying the resulting array by $33 \text{ cm}^2 \text{ s}^{-2}$.

Figure 14 also shows the potential perturbations associated with all three density waves derived using this procedure. For each wave, we also include a horizontal dashed line corresponding to the expected value of the gravitational perturbation potential (33, 30, and $21 \text{ cm}^2 \text{ s}^{-2}$, respectively; see Tiscareno & Harris 2018). For both the Mimas 6:2 and Pandora 4:2 waves, the relative amplitudes stay within 50% of their expected values, while for the Prometheus 4:2 wave the curves deviate from the expected value a bit more, most likely because of the lower signal-to-noise for this wave. Still, these results show that this procedure

⁸ This range was smaller than the others to exclude the signals from the stronger Mimas 6:2 wave.

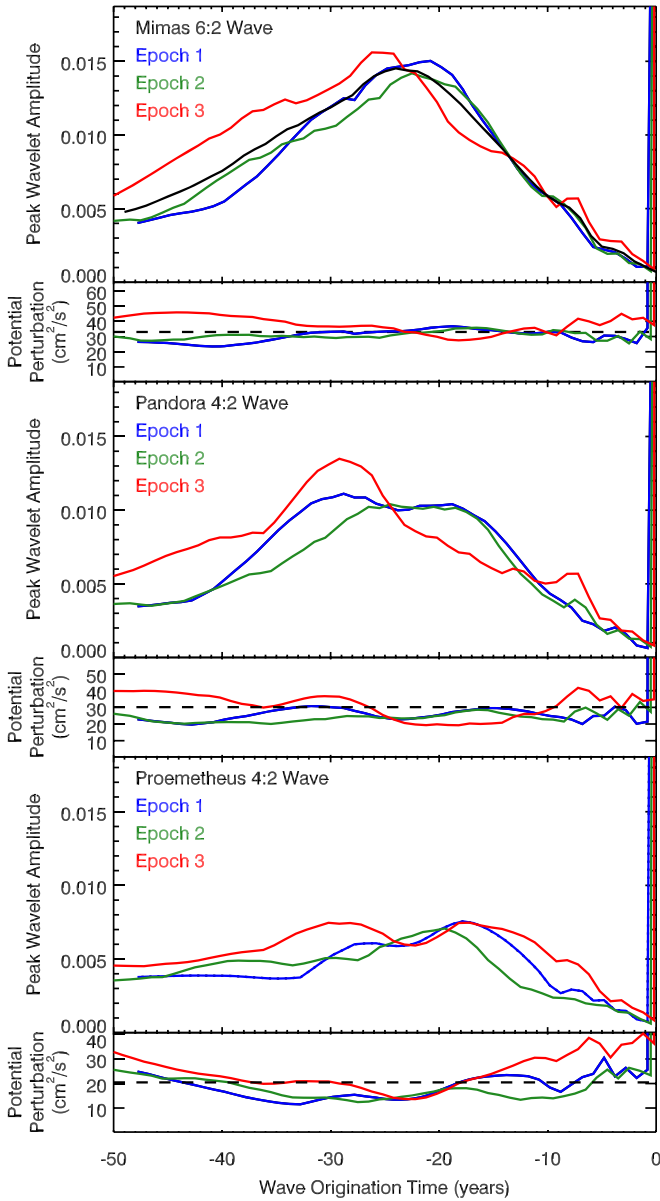


Figure 14. Plots of the peak wavelet amplitude A_w and inferred gravitational potential perturbation amplitude Φ'_3 as a function of δt for three $m = 3$ satellite waves for the three observation epochs. For the Mimas 6:2 wave, the top panel shows the measured peak wavelet amplitudes A_w from the three observation epochs, along with the average of the three profiles. The second panel shows the estimated gravitational potential perturbation amplitudes Φ'_3 based on this template. The other panels show the observed peak wavelet amplitudes and derived potential perturbation amplitudes for the weaker Pandora and Prometheus 4:2 waves.

yields reasonable estimates of the gravitational perturbations responsible for producing density waves in the C ring.

Of course, the conversion factors derived from the Mimas 6:2 wave may not be perfectly accurate for other waves, because a wave's amplitude not only depends on Φ'_m , but also on local ring properties like the surface mass density and effective viscosity (see the [Appendix](#)). Fortunately, since the Mimas 6:2 wave occupies a similar environment as the planet-generated waves, these potential inaccuracies are more manageable. In particular, the background surface mass densities for all of the waves considered here are between 0.6 and 2.0 g cm⁻² (see [Table 2](#)). Standard models predict that the conversion factor should scale like $\sigma_0^{-1/2}$ (see Equation (64) in the [Appendix](#)), so the observed

Table 3

Normalization Curves Based on the Average Signal from the Mimas 6:2 Wave

Elapsed Time	A	Elapsed Time	A	Elapsed Time	A
0	0.000 70	20	0.013 42	40	0.007 56
1	0.001 06	21	0.013 96	41	0.007 19
2	0.001 42	22	0.014 32	42	0.006 81
3	0.001 97	23	0.014 39	43	0.006 43
4	0.002 27	24	0.014 52	44	0.006 12
5	0.002 42	25	0.014 32	45	0.005 83
6	0.003 14	26	0.013 99	46	0.005 49
7	0.004 36	27	0.013 43	47	0.005 20
8	0.005 07	28	0.012 69	48	0.004 97
9	0.005 39	29	0.012 30	49	0.004 77
10	0.005 84	30	0.011 86		
11	0.006 49	31	0.011 53		
12	0.007 24	32	0.011 11		
13	0.008 07	33	0.010 66		
14	0.008 94	34	0.010 39		
15	0.009 71	35	0.009 17		
16	0.010 49	36	0.009 39		
17	0.011 27	37	0.009 03		
18	0.012 08	38	0.008 60		
19	0.012 77	39	0.008 05		

variations in the surface mass density across these rings should only affect the Φ'_m estimates by at most 50%. Variations in the effective ring viscosity across the middle C ring turn out to have a more noticeable effect on the particular waves considered here. Fortunately, inaccuracies in the conversion due to viscosity variations can be identified because they cause time-dependent changes in the conversion factors (see Equations (64) and (65) in the [Appendix](#)). Errors in the assumed viscosity therefore result in diagnostic disagreements among estimates of Φ'_m derived from data obtained at different times. Such disagreements will be noted when they occur.

3.4. Summary and Validation of Analytical Procedures

Figures 15 and 16 summarize the outputs of the full wavelet analyses described above for the three $m = 3$ satellite waves. These plots include the relevant parts of the \mathcal{R}^{\max} (signal-to-noise) and Φ'_m (gravitational potential perturbation) arrays derived from the three epochs as functions of wave formation time and initial pattern speed. Note that data are only included where the normalization curve in [Table 3](#) is above 0.25 its peak value, because for the data outside this region uncertainties in the normalization dominate the visible appearance of the maps. The three waves appear as nearly vertical bands in both \mathcal{R}^{\max} and Φ'_m , consistent with each perturbation having a fixed frequency. There is a slight slope in the Mimas wave at 763° day⁻¹ in [Figure 15](#) that most likely reflects the slight difference in the background surface mass densities for these two waves in this region ([Baillié et al. 2011](#)). Also note that the variations in the background outside of these vertical bands have a common tilt that arises from translating the observed location of the features to the initial pattern speed of the perturbation.

These figures also show the peak values of the \mathcal{R}^{\max} and Φ'_m arrays in the selected regions as functions of formation time. The peak amplitudes Φ'_m are roughly the same over the entire time span, consistent with the constant potential perturbations between 20 and 33 cm² s⁻² associated with these waves. For the Prometheus 4:2 wave shown in [Figure 16](#), the signal-to-noise

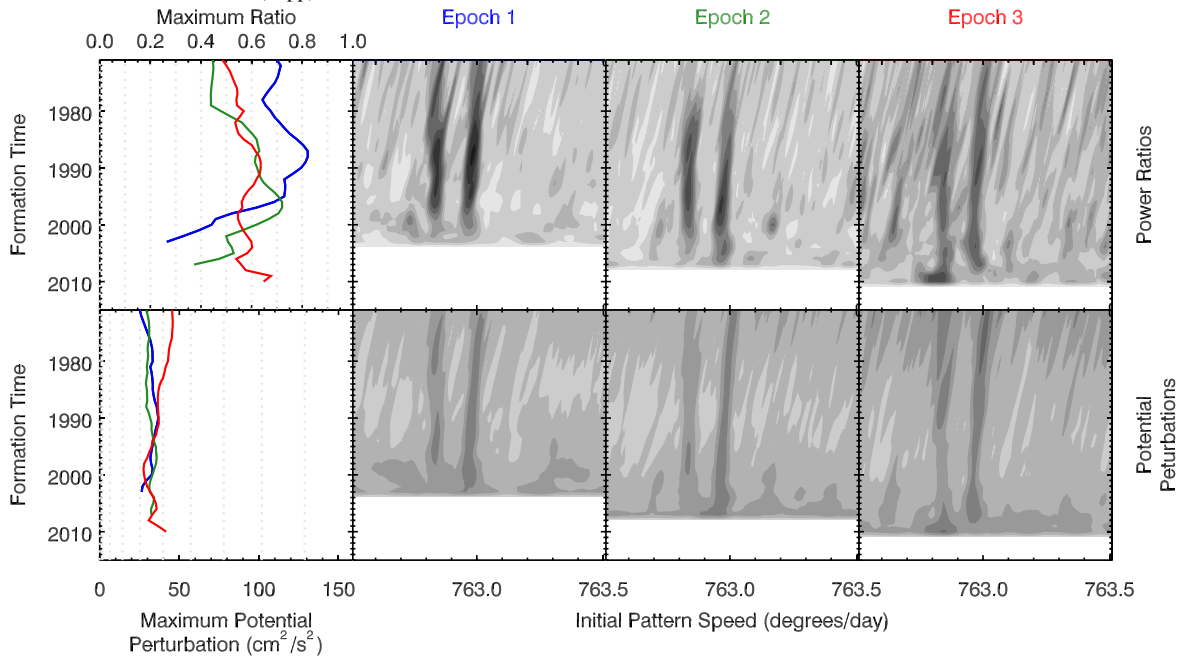


Figure 15. The results of the wavelet analysis of the Mimas 6:2 and Pandora 4:2 waves. The top row shows the power ratios \mathcal{R}^{\max} as functions of initial pattern speed and formation time, while the bottom row shows the estimated potential perturbations Φ'_m . Each of the right three panels shows the arrays derived from one of the Cassini epochs, while the left panels show the peak values of \mathcal{R}^{\max} and Φ'_m as functions of formation time. Note that the gray dotted lines in the left panels correspond to the grayscale levels in the corresponding images. Also, data are only displayed for times where the normalization curve is at least 0.25 its peak value. In this case, the two vertical bands in the images correspond to the perturbations from the Pandora 4:2 resonance at $762^{\circ}8 \text{ day}^{-1}$ and the Mimas 6:2 resonance around $762^{\circ}9 \text{ day}^{-1}$. Note that the amplitudes of these signals are roughly constant around $30 \text{ cm}^2 \text{ s}^{-2}$, and the pattern speeds do not change much with time, consistent with standard satellite resonances.

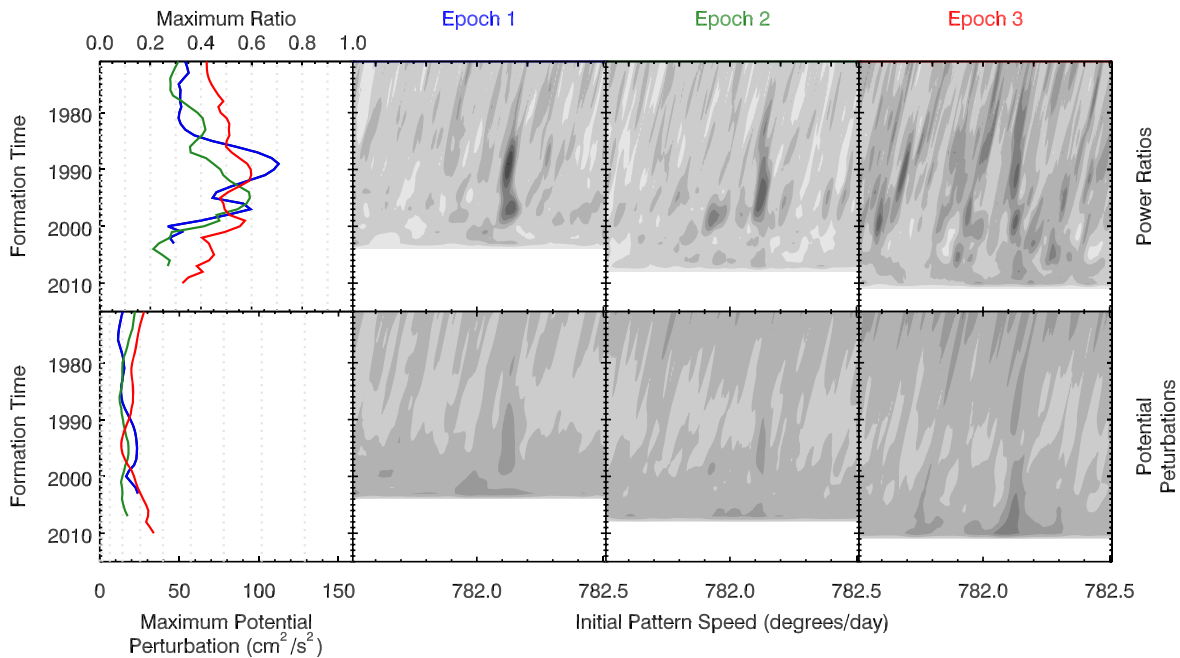


Figure 16. The results of the wavelet analysis of the Prometheus 4:2 wave in the same format as Figure 15. In this case, the vertical bands in the wavelet maps correspond to the signal from the Prometheus 4:2 resonance at $782^{\circ}1 \text{ day}^{-1}$. Note that the amplitude of this signal is roughly constant around $20 \text{ cm}^2 \text{ s}^{-2}$, and the pattern speeds do not change much with time, consistent with a standard satellite resonance.

is considerably lower than it is for the other two waves, consistent with the wave’s lower amplitude. However, the wave signal is fairly clear in the \mathcal{R}^{\max} arrays between 1990 and 2000, and a weak enhancement in Φ'_m is also visible at these locations. This implies that the lower limit on detectable perturbations is around this level in these regions.

4. Results

The transformations described in Section 3.3 above yield maps of the perturbation amplitudes associated with the various Saturn-generated waves as functions of perturbation period and time. When considering these plots, it is important to remember that the Φ'_m estimates are likely only accurate to around 50% for

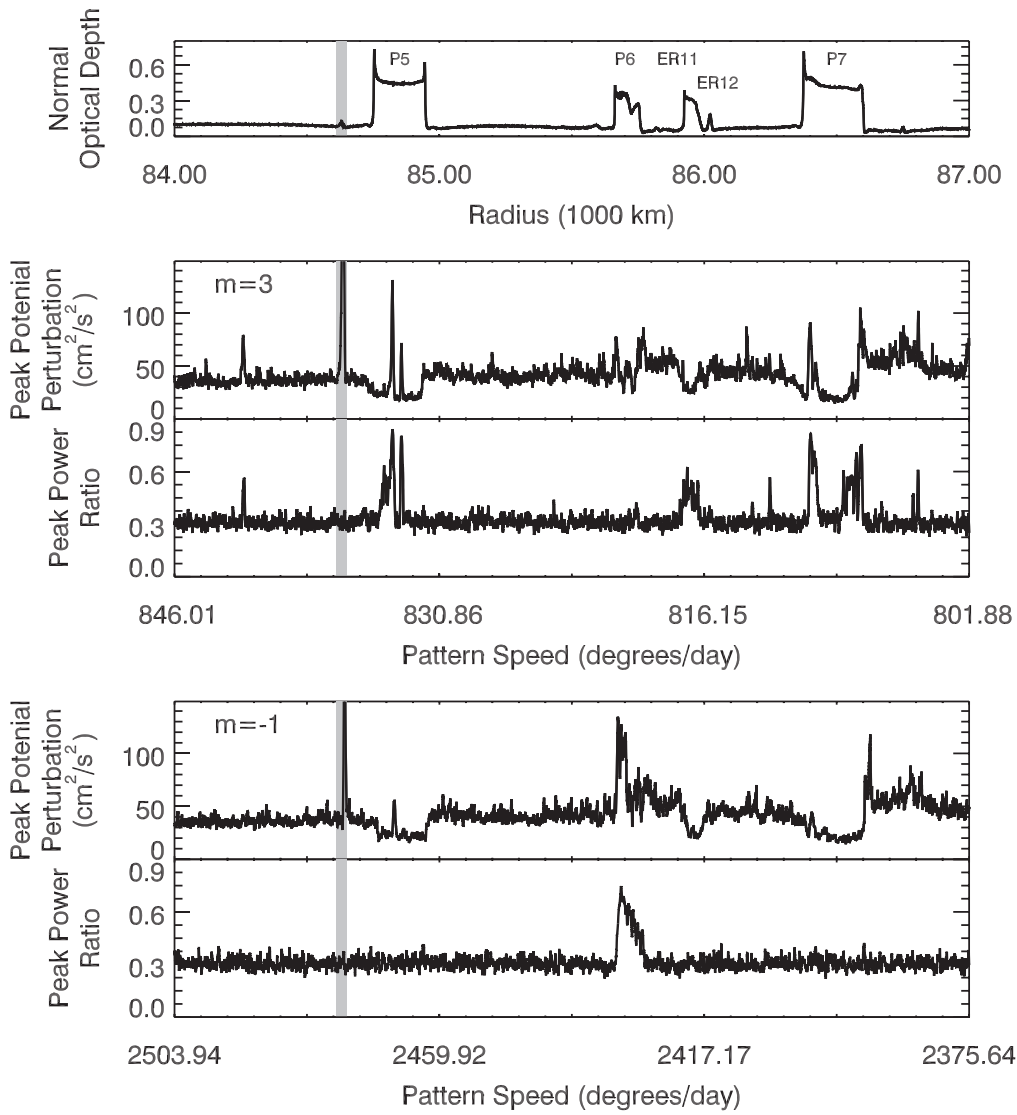


Figure 17. An overview of the $m = 3$ and $m = -1$ waves in the middle C ring. The top panel shows an optical depth profile of the rings, while the lower panels show the peak values of the potential perturbation Φ'_m and power ratio \mathcal{R}^{\max} for elapsed times between 7 and 40 yr as functions of the corresponding initial pattern speed of the waves (the plotted curves are the averages of the data from the three epochs, since the differences between the epochs were generally small). The gray shaded band in these plots corresponds to the W84.64 wave, which contaminates the Φ'_m profiles.

waves in regions similar to those occupied by the satellite waves. Furthermore, as will be discussed in more detail below, there is evidence that the regions between the plateaux and the $m = -1$ wave may have different dissipation properties that may introduce further systematic uncertainties in the inferred perturbation strengths. Despite these limitations, these maps provide useful information about the recent history of these various gravitational perturbations.

The signals from individual features will be discussed in detail below. However, it is first worth examining the overview of the locations and pattern speeds of the $m = 3$ and $m = -1$ signals shown in Figure 17. For the sake of clarity, this plot just shows the peak values of the power ratio and Φ'_m as functions of radius and the corresponding initial pattern speeds, assuming a constant surface mass density of 1.3 g cm^{-2} . The power ratio profiles show a uniform background level, and so provide clearer information about the locations of the wave signals. Meanwhile, the Φ'_m profiles indicate the relative strength of the perturbations responsible for making these features.

The $m = 3$ signals in Figure 17 have roughly the same distribution as the signals shown in Figure 10. The strongest wave signals are observed in the middle of the plateau known as P5 around 84,800 km and on either side of the P7 plateau at 86,400 km. The peak potential perturbations for all three of these regions are above $50 \text{ cm}^2 \text{ s}^{-2}$. These correspond to the previously identified $m = 3$ wave signals designated W84.82, W84.86, W86.40, W86.58, and W86.59 by Hedman & Nicholson (2014). Meanwhile, in the $m = -1$ profile, there is a single clear signal with a correspondingly large peak perturbation amplitude in the P6 plateau at 85,700 km, which corresponds to the wave previously designated as W85.67.

In addition to these previously known wave signals, the plateau-like feature ER11 at 85,950 km also shows elevated power ratios, but no obvious signals in the perturbation potential amplitudes (in fact, the peak perturbations are lower in this plateau than they are in the surrounding C ring). The lack of obvious peaks in the perturbation amplitude implies that the perturbations responsible for these signals are well below

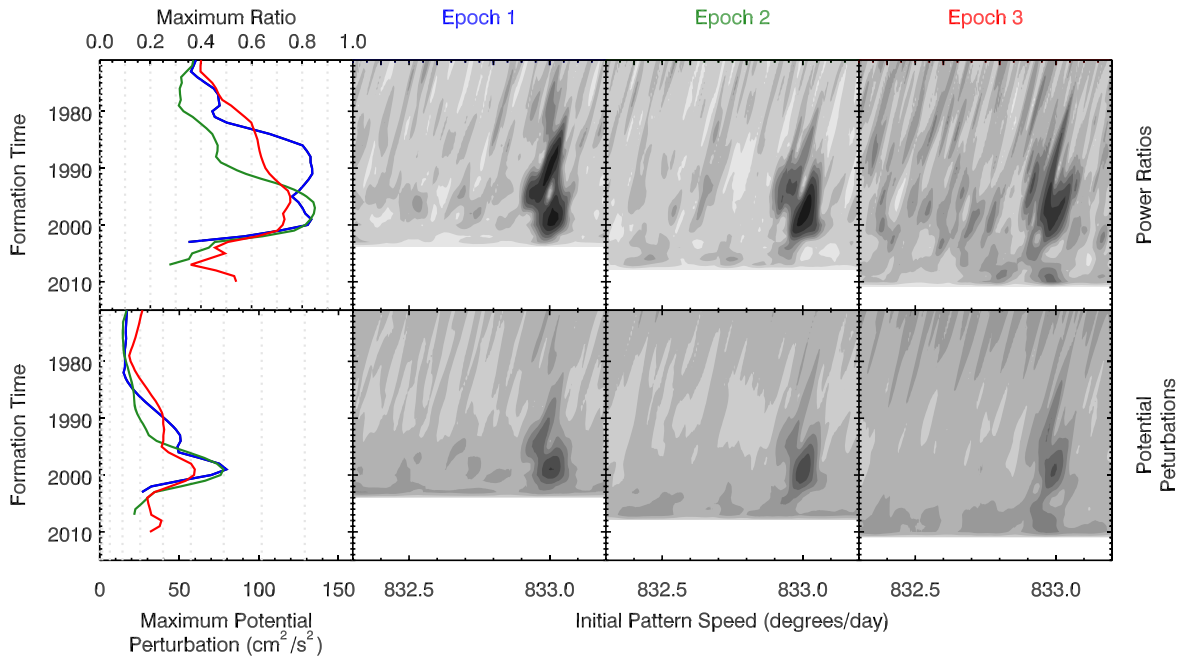


Figure 18. The results of the wavelet analysis of the region around wave W84.86 in the same format as Figure 15. For all three epochs, there is a clear peak in the perturbation amplitude at a pattern speed of 833.0 day^{-1} that started sometime in the 1980s, reached a peak value of around $70 \text{ cm}^2 \text{ s}^{-2}$ in 1999, and then dissipated around 2003.

$50 \text{ cm}^2 \text{ s}^{-2}$, and so are substantially weaker than the previously identified $m = 3$ waves.

More generally, it appears that the background Φ'_m levels are higher in the background C ring than inside the plateaux, most likely because of differences in the fine-scale structures of these regions. Hence, weak wave signals might be harder to discern outside of the plateaux. Still, there are narrow peaks in several locations between the plateaux corresponding to pattern speeds of around 804° , 812.5° , 813.5° , and $842^\circ \text{ day}^{-1}$ (another weak peak around $820^\circ \text{ day}^{-1}$ is an alias of the $m = -1$ wave). By contrast, the $m = -1$ profiles show no obvious additional signals beyond W85.67.

For the sake of clarity, our discussion of the individual wave features will begin with the strong $m = 3$ signals. First, we will examine the features around $84,800 \text{ km}$ that turn out to represent short-lived asymmetries in the planet's gravitational field. We will then consider the longer-lived feature around $86,400 \text{ km}$, along with the $m = -1$ wave W85.67, and present evidence that both of these waves likely have a common origin. Next, we will discuss the structures found around $86,600 \text{ km}$ and show that these include both long-lived and transient perturbations. After that, we will examine the weak patterns around $85,900 \text{ km}$, and, finally, we will discuss the narrow $m = 3$ signals between the plateaux.

4.1. Short-lived Perturbations between 832° and $834^\circ \text{ day}^{-1}$

Figures 18 and 19 show the results of our wavelet analysis for the regions around the waves W84.86 and W84.82, respectively. We can first consider the signals around W84.86 because these are the simpler of the two. The wavelet maps show a clear signal in both the power ratios and the perturbation amplitudes, but unlike the satellite-driven density waves shown in Figures 15 and 16, these signals do not have constant amplitudes for all times. Instead, in this case, it appears that the amplitude of the perturbation slowly grew from

a low value in the mid-1980s to a peak value of around $70 \text{ cm}^2 \text{ s}^{-2}$ in 1999, before fading away again over the next few years. Note that the detailed shape of this peak is smoothed somewhat by the finite wavenumber resolution of the wavelet transform, so the actual perturbation may not have fallen as smoothly after 1999 as the curves shown in Figure 18 suggest. However, close inspection of the wavelets does reveal substructure in the signal that could indicate that there were actually two different perturbations: a weaker, longer-lived one, extending between the early 1980s and roughly 1995, and a stronger, shorter-lived anomaly that was strongest in 1999. Note that this substructure is visible in the data from all three epochs, with only slight differences that probably represent differences in the effective wavenumber resolution. This not only supports the reality of these particular temporal trends, but also demonstrates how much information these waves contain about the recent history of perturbations on the ring.

The region around W84.82 shown in Figure 19 reveals a considerably more complicated perturbation history. First of all, all three epochs show evidence of a perturbation around 833.5 day^{-1} that rapidly grew in the mid-1990s to a peak value of around $120 \text{ cm}^2 \text{ s}^{-2}$ in 1999, before fading away over the next few years. However, the later Cassini data show that a signal at this same frequency reappeared and again reached a maximum perturbation amplitude of around $120 \text{ cm}^2 \text{ s}^{-2}$ in 2008, before starting to fade again. Furthermore, besides the very strong signal at 833.5 day^{-1} , additional wave signals can be seen at initial pattern speeds between 833.7 and 834.1 day^{-1} , which generally have amplitudes of around $30\text{--}40 \text{ cm}^2 \text{ s}^{-2}$. The earliest of these weaker signals occurs around 833.7 day^{-1} in the 1980s, and is most clear in the data from Epochs 1 and 2. Then, in the 1990s, there appear to be four or five wave signals with comparable strength between 833.7 and 834.1 day^{-1} . Finally, the data from Epochs 2 and 3 show a weak wave signal around 833.7 day^{-1} that is strongest around 2005, when the 833.5 day^{-1} signal is weakest.

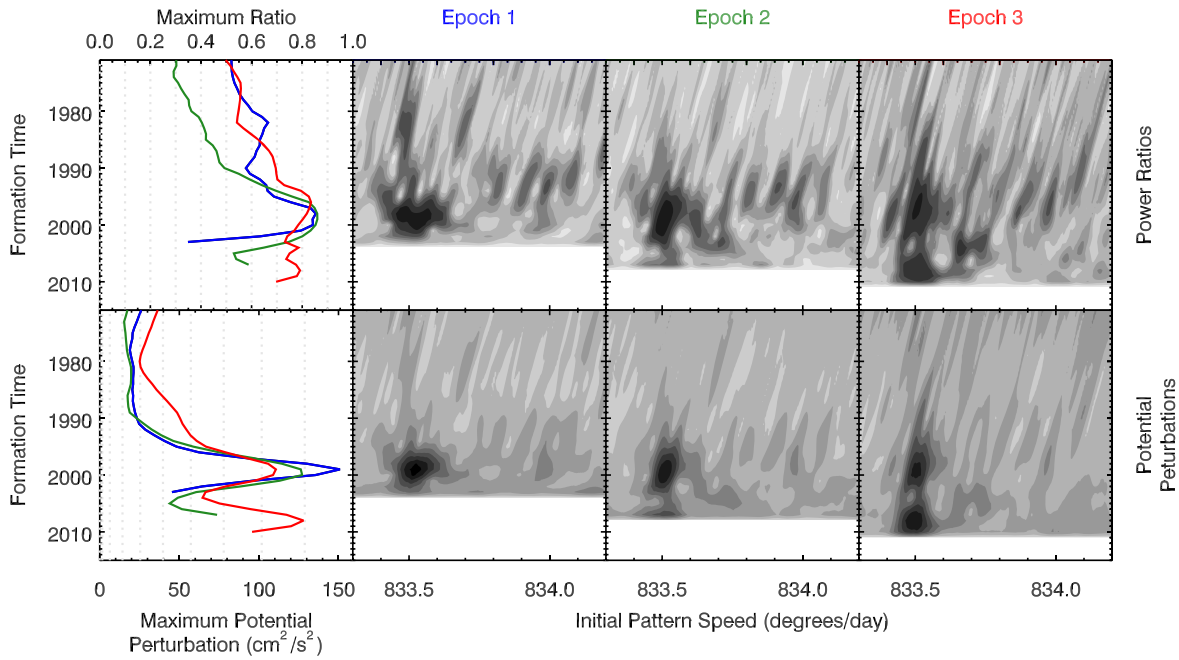


Figure 19. The results of the wavelet analysis of the region around wave W84.82 in the same format as Figure 15. The strongest signals here are around 833.5 day^{-1} . For all three epochs, we see a signal in the perturbation amplitude that first appeared in the late 1990s, before reaching a peak of around $120 \text{ cm}^2 \text{ s}^{-2}$ in 1999. This signal faded significantly in the early 2000s, but the data from Epochs 2 and 3 show that it reappeared a few years later, probably peaking again in 2008. In addition to these particularly strong signals, there is also a series of weaker signals between 833.7 and 834.1 day^{-1} that appear to have been most active in the 1990s, and other signals around 833.7 day^{-1} that were most active in the 1980s and early 2000s.

This region therefore provides evidence for multiple short-lived signatures. Furthermore, it appears that in this region the strongest perturbations occurred around 1999, but a larger number of somewhat weaker perturbations occurred in the decade before this, and one strong perturbation occurred about a decade later.

4.2. A Long-term Perturbation with a Drifting Pattern Speed around $810^\circ \text{ day}^{-1}$ and $2430^\circ \text{ day}^{-1}$

In stark contrast to the patterns between 832° and $834^\circ \text{ day}^{-1}$, the perturbation around $810^\circ \text{ day}^{-1}$ responsible for the wave designated W86.40 has apparently existed for many decades. However, as shown in Figure 20, the pattern speed of this perturbation has steadily increased from 810° to 810.5 day^{-1} between 1970 and 2010. Note that this relatively steady shift in pattern speed extends over a time period greater than a Saturn year, so this drift cannot be attributed to seasonal changes in Saturn’s atmosphere.

In addition to the rather steady evolution in pattern speed, the data from the three epochs also show very consistent variations in the amplitude of the pattern. First of all, the perturbation amplitude seems to decline from around $50 \text{ cm}^2 \text{ s}^{-2}$ in the 1970s to around $30 \text{ cm}^2 \text{ s}^{-2}$ around 1988. The perturbation amplitude then grows back to around $50 \text{ cm}^2 \text{ s}^{-2}$ in the early 1990s. This is followed by a short reduction in the perturbation strength around 1997 that appears as a relatively narrow vertical gap in the two-dimensional maps at 810.25 day^{-1} , but is not well resolved in the curves showing peak signals due to the finite vertical extent of the signal band. Finally, the signal grows again to a broad peak of around $100 \text{ cm}^2 \text{ s}^{-2}$ sometime in the 2000s, before it starts to decay one last time.

Surprisingly, the trends in pattern speed and perturbation amplitude seen in the $m = 3$ wave W86.40 are very similar to the trends seen in the $m = -1$ wave W85.67 shown in

Figure 21. First of all, the pattern speed associated with this wave also steadily increases with time between 1970 and 2010, going from a bit under 2430° to about 2431.5 day^{-1} , so over these four decades the pattern speed of this perturbation is almost exactly three times the pattern speed of the perturbation responsible for W86.40 (and any small discrepancies in this relationship can potentially be explained by small differences in the local surface mass density). Turning to the perturbation amplitudes, we can note that the curves derived from different epochs are less consistent in this case than they were for W86.40, which suggests that the normalization curve that works well for the previous $m = 3$ waves is not quite as appropriate for this particular wave. However, close inspection of the wavelets still shows evidence for local minima in the perturbation amplitudes around 1990 and 1997. Note that while the 1997 minima are fairly clear in the Epoch 1 and 2 data, the 1990 minima are less clear than they are in the $810^\circ \text{ day}^{-1}$ wave, because the $m = -1$ waves propagate in the opposite direction as the pattern speed is changing, which makes the waves generated at different times more likely to overlap each other (see also Figure 11).

W85.67 is the only one of the waves discussed here that was also observed by the Voyager spacecraft (Rosen et al. 1991), and so in Figure 22 we include a wavelet map derived from the Voyager Radio Science Subsystem (RSS) occultation profile available on the Planetary Data System Ring-Moon Systems Node with a nominal resolution of 200 m. Of course, with a single occultation, we cannot compute the power ratio \mathcal{R} , but we can still use the wavelet transform of these occultation data to estimate A_w and the corresponding gravitational perturbation Φ'_m . As shown in Figure 22, the Voyager data are also consistent with a steadily increasing pattern speed over time, and the pattern speed in 1970 is around $2430^\circ \text{ day}^{-1}$, which matches the Cassini observations. We can therefore say that a perturbation with a steadily increasing pattern speed ($2429.5 \text{ day}^{-1} < \Omega_p < 2431.5 \text{ day}^{-1}$) has existed for at least 50 yr, from 1960 through 2010.

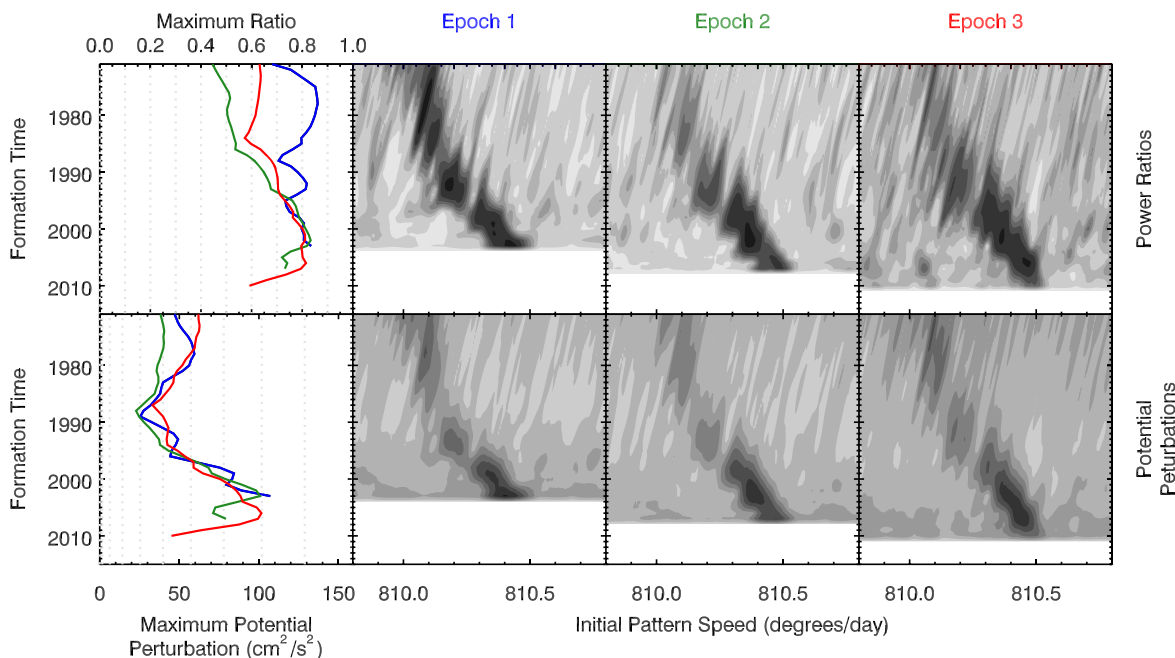


Figure 20. The results of the wavelet analysis of the region around the $m = 3$ wave W86.40 in the same format as Figure 15. In this case, there appears to be a single perturbation that has existed since 1970 and whose pattern speed has steadily increased over four decades from 810° to 810.5 day^{-1} . Note that the amplitude of the perturbation has changed substantially over time, decreasing to a minimum of around $30 \text{ cm}^2 \text{ s}^{-2}$ around 1990, rising to a value of around $50 \text{ cm}^2 \text{ s}^{-2}$ around 1994, then falling briefly again before reaching a maximum of around $100 \text{ cm}^2 \text{ s}^{-2}$ in the mid-2000s.

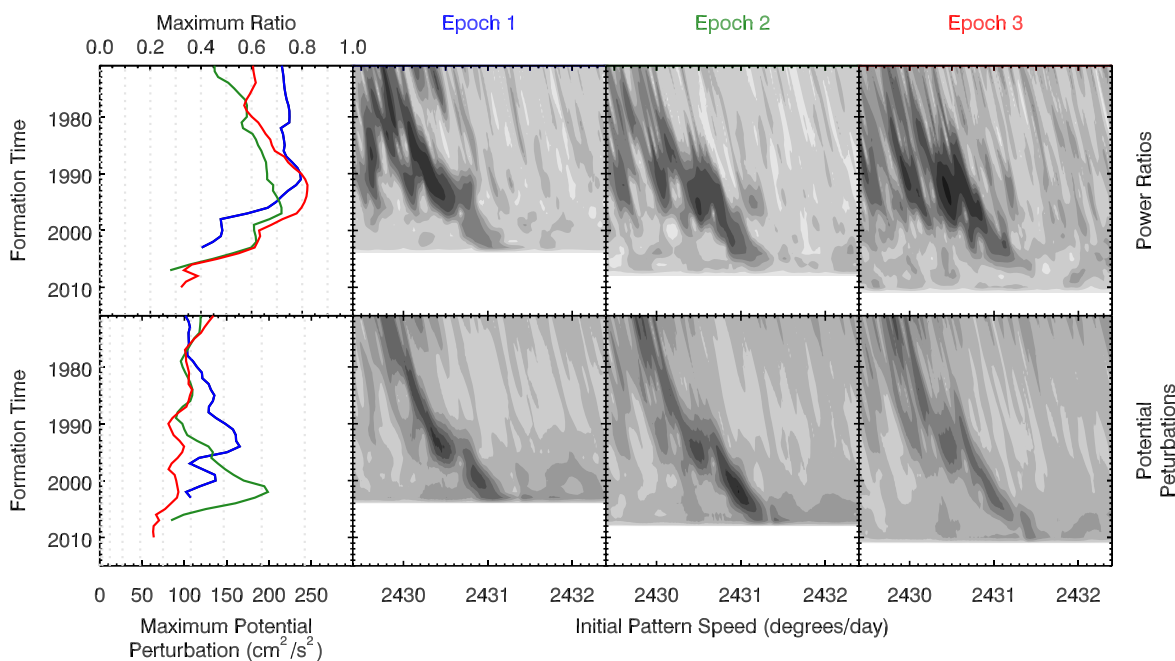


Figure 21. The results of the wavelet analysis of the region around the $m = -1$ wave W85.67 in the same format as Figure 15. These data show evidence of a continuous disturbance whose pattern speed has steadily changed between 2430° and 2431.5 day^{-1} between 1970 and 2010. Note that the amplitudes of the perturbations derived from the different epochs are more discordant than those shown in Figure 20, indicating that the normalization model may not be ideal here. Even so, one can see local minima in the perturbation amplitudes around 1990 and 1997 that are very similar to those seen in Figure 20, indicating that these waves may share a common origin.

If we use the same normalization curves as we have used for the $m = 3$ waves on all of these profiles, we find an estimated perturbation amplitude in the 1980s from the Cassini data that is well below that observed in the Voyager data. This suggests that the normalization curve derived from the Mimas 6:2 wave is not exactly appropriate for this wave. After some experimentation, we found that if we scaled the normalization curve in time by a factor of 80% (i.e., reducing the effective

dissipation time to around 29 yr), this not only improved the match between the Cassini and Voyager estimates of the perturbation strength in the 1970s, but also improved the match among the various Cassini epochs. With this revised normalization, it appears that the perturbation amplitude was substantially higher in the 1970s and 1980s than it has been more recently. The Voyager data also indicate that the perturbation was significantly weaker before 1960. However,

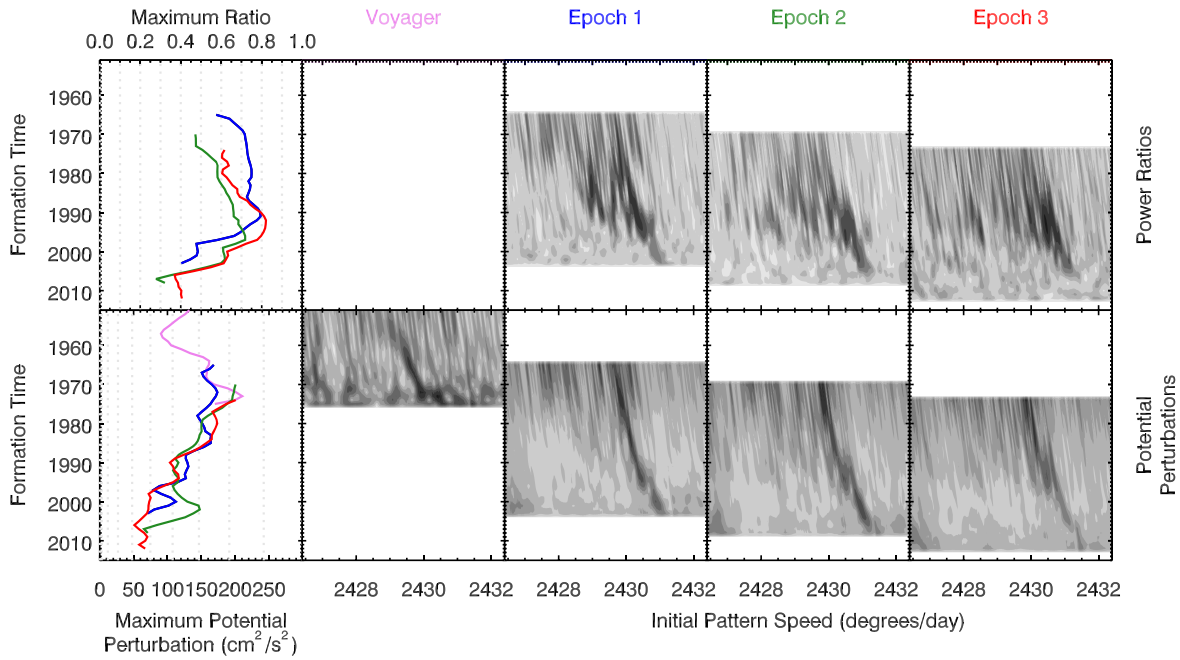


Figure 22. The results of the wavelet analysis of an extended region around the $m = -1$ wave W85.67 in the same format as Figure 15, except that it includes data from the Voyager RSS occultation, and the amplitudes are normalized using a template scaled by 80% in elapsed time. With this normalization, the amplitude of the perturbation appears to have declined over the past four decades. Also, the Voyager data allows us to extend the time evolution of this perturbation back to 1960. Also note that weaker signals can be seen between 2427° and $2430^\circ \text{ day}^{-1}$ in the 1980s and 1990s.

this edge probably actually reflects the finite spatial resolution of the Voyager radio occultation experiment, and so we cannot currently make any firm conclusions about the strength of this perturbation prior to 1960.

The broader span of the pattern speeds in Figure 22 also reveals that, in addition to the perturbation with the steadily increasing pattern speed, there are also several weaker signals in the 1970s through the early 1990s at pattern speeds between 2427° and $2430^\circ \text{ day}^{-1}$ that can be seen most clearly in the power ratios. These signals are rather patchy, and their locations are not always repeatable among the various epochs, which is similar to the weak $m = 3$ signals around $817^\circ \text{ day}^{-1}$ discussed below.

In summary, the similar trends in the pattern speeds and the coincident minima in the perturbation amplitudes around 1990 and 1997 strongly suggest that W86.40 and W85.67 are created by the same structure in Saturn’s gravitational field. This connection is also supported by the fact that the pattern speed of the $m = -1$ pattern is always three times the pattern speed of the $m = 3$ pattern, which means the frequency of the two perturbations for an inertially fixed observer $\omega = |m|\Omega_p$ is the same for both waves. However, it is important to keep in mind that there are also important differences between the two signals. First of all, the amplitude of the $m = 3$ perturbation seems to have generally increased over time since the 1980s, while the amplitude of the $m = -1$ perturbation has either decreased (if the normalization used in Figure 22 is correct) or stayed roughly constant (if the normalization used in Figure 21 is more accurate). Also, there are no secondary perturbations around the $m = 3$ pattern like there are around the $m = -1$ pattern.

4.3. Persistent and Transient Disturbances around $808^\circ \text{ day}^{-1}$

Figure 23 shows the wavelet analysis of a region that contains the wave features identified by Hedman & Nicholson (2014)

as W86.58 and W86.59. The most prominent and persistent signals in this region are between $807^\circ.6$ and $807^\circ.7 \text{ day}^{-1}$, which correspond to the wave W86.59. The signals in this region appear to have multiple components with amplitudes around $50 \text{ cm}^2 \text{ s}^{-2}$.⁹ In Epochs 2 and 3, there appear to be two closely spaced signals separated by only $0^\circ.05 \text{ day}^{-1}$ prior to 1995. More recently, the amplitude of the signal may oscillate between 50 and $70 \text{ cm}^2 \text{ s}^{-2}$ over timescales of about a decade. Despite this variability, the amplitude and pattern speed of this particular structure appears to be more stable than any of the perturbations considered thus far.

By contrast, between $807^\circ.9$ and $808^\circ.4 \text{ day}^{-1}$, there are series of weaker and more transient perturbations. The most prominent of these signals are of order $40 \text{ cm}^2 \text{ s}^{-2}$ and include patches at around $807^\circ.9 \text{ day}^{-1}$ in 1995 and 2000, as well as another patch around $808^\circ.1 \text{ day}^{-1}$ in 2004. Weaker signals between $808^\circ.2$ and $808^\circ.4 \text{ day}^{-1}$ are seen in the 1990s, and there may also be a weak signal around $808^\circ.2 \text{ day}^{-1}$ in 1980.

4.4. Weak Transient Perturbations around $817^\circ \text{ day}^{-1}$

Turning to the weaker signals around $817^\circ \text{ day}^{-1}$ (i.e., around 85,900 km in radius), Figure 24 shows that there are no obvious signals stronger than $30 \text{ cm}^2 \text{ s}^{-2}$ in this region. However, there are patchy signals in \mathcal{R}^{max} distributed between $816^\circ.5$ and $817^\circ.3 \text{ day}^{-1}$. Most of these signals appear to have been active between 1980 and 2000. The one potential exception is a signal in $817^\circ.2 \text{ day}^{-1}$ that might have been active in 2008, which is only seen in the Epoch 3 data.

⁹ A more intense signal around $807^\circ.6 \text{ day}^{-1}$ seen only in the Epoch 3 wavelet map, which causes the estimated perturbation potential amplitude to climb above $100 \text{ cm}^2 \text{ s}^{-2}$, is not a real $m = 3$ signal because it corresponds to a low value of \mathcal{R}^{max} .

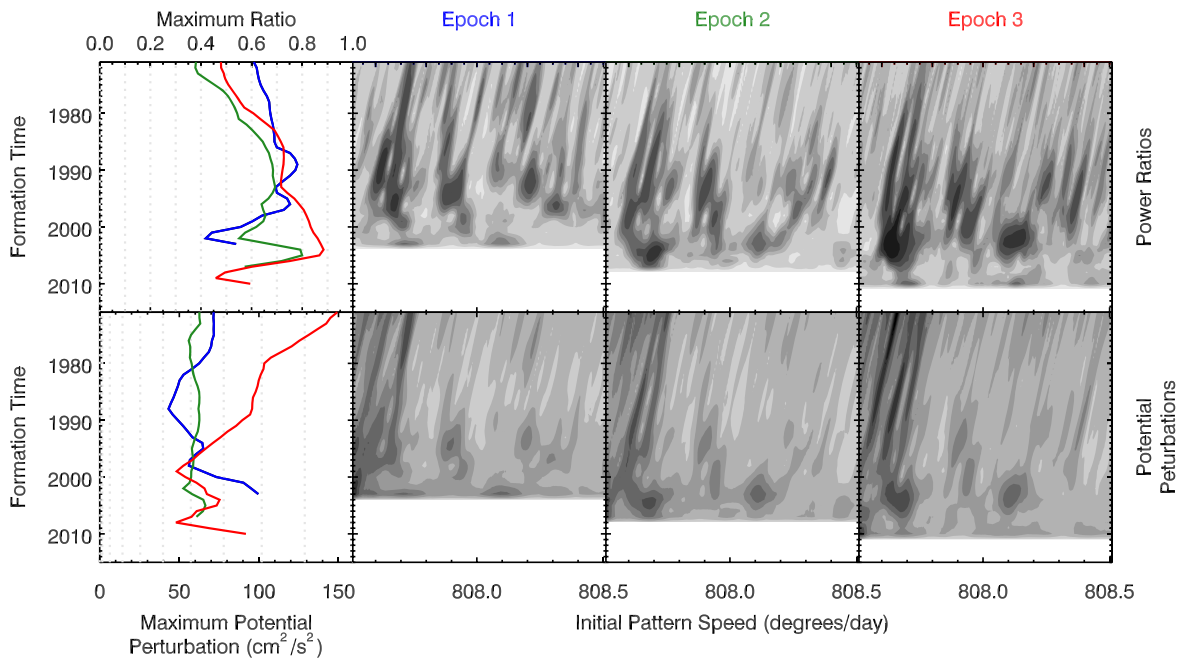


Figure 23. The results of the wavelet analysis applied to the region around W86.58 and W86.59 in the same format as Figure 15. In this case, the more prominent and persistent signal is around $807^{\circ}6 \text{ day}^{-1}$, which may have subcomponents and variations over time. In addition, weaker and more transient signals can be seen in the 1990s through early 2000s between $807^{\circ}9$ and $808^{\circ}4 \text{ day}^{-1}$.

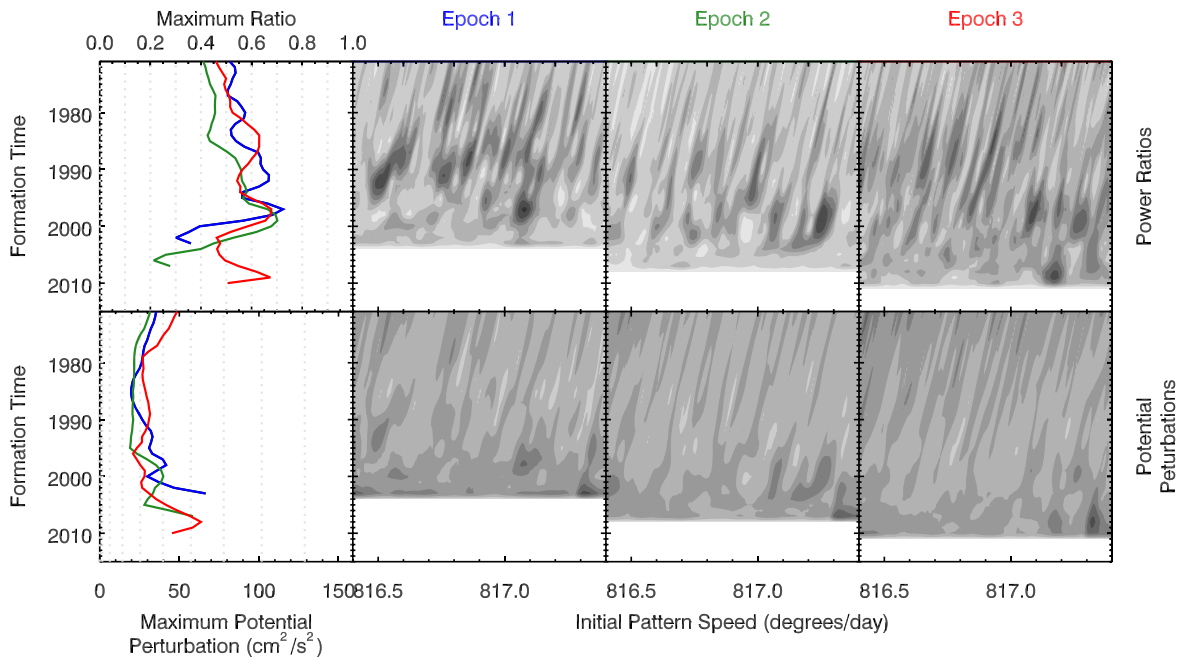


Figure 24. The results of the wavelet analysis on the perturbations between $816^{\circ}5$ and $817^{\circ}3 \text{ day}^{-1}$ in the same format as Figure 15. In this case, there is not much visible in the perturbation amplitude, but patchy signals can be seen in the power ratio.

4.5. $m = 3$ Wave Signals outside of Plateaux

Finally, we can consider the $m = 3$ wave signatures found outside the plateaux. Note that unlike the more complex signatures found inside the various plateaux, these features are more consistent with individual waves, and will therefore be designated as such based on their radial locations within the rings, consistent with prior work (Hedman & Nicholson 2013, 2014; French et al. 2016, 2019; Hedman et al. 2019; French et al. 2021).

First of all, Figure 25 shows that between $804^{\circ}5$ and $805^{\circ}0 \text{ day}^{-1}$ there are two discrete wave signals that are located

at radii around 86,800 km, just outside the rightmost plateau (P7) in Figure 17. The stronger one, at $804^{\circ}6 \text{ day}^{-1}$, is designated W86.81, while the weaker signal at $804^{\circ}8 \text{ day}^{-1}$ is designated W86.79. There are no obvious variations in the pattern speeds of these structures. The peak perturbation amplitudes for W86.81 are consistently around $100 \text{ cm}^2 \text{ s}^{-2}$, while those from W86.79 are closer to $50\text{--}60 \text{ cm}^2 \text{ s}^{-2}$, which is close to the background variations in this region. For W86.81, the perturbation amplitude appears to increase over time, but close inspection of the trends indicates that this increase happens at different times for the

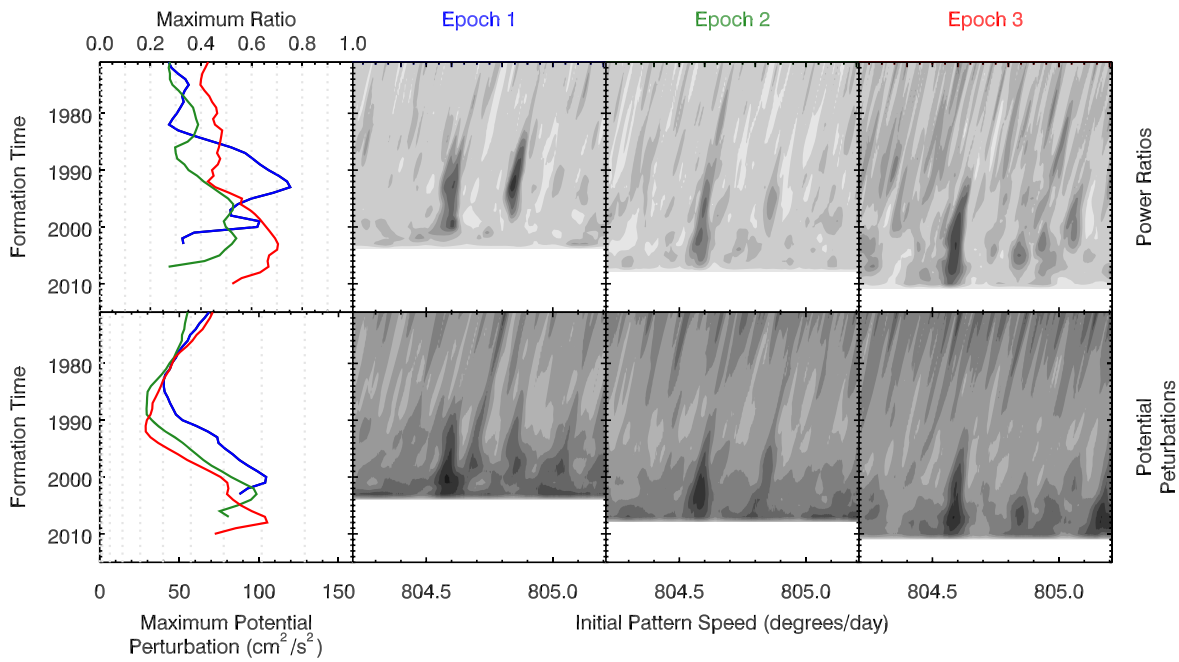


Figure 25. The results of the wavelet analysis of the waves W86.81 and W86.79 in the same format as Figure 15. In this region, all three epochs contain a signal at around $804^{\circ}6 \text{ day}^{-1}$ with a relatively constant pattern speed, which we identify with the wave W86.81. Another, weaker signal is seen at $804^{\circ}8 \text{ day}^{-1}$, which corresponds to the wave W86.79.

different epochs, which is inconsistent with a true change in the perturbation amplitude. Instead, these apparent variations likely arise because waves dissipate faster outside of the plateaux than they do inside the plateaux, causing the estimated signals to artificially decay in the past.

Ideally, we could use density waves outside the plateaux to derive normalization curves for these features, but there are no known $m = 3$ waves outside of the plateaux that can be used for this purpose. We will therefore just highlight that the amplitudes of these perturbations are less reliable than those for waves found inside the plateaux. More specifically, since dissipation seems to be stronger outside of the plateaux, the perturbation amplitudes in these regions are likely underestimated.

Moving on, Figures 26 and 27 show similar plots for the waves with pattern speeds around $812^{\circ}6$ and $813^{\circ}5 \text{ day}^{-1}$ located around 86,200 km and interior to the outermost plateau (P7) in Figure 17. We designate these features as W86.25 and W86.18, respectively. The signal from W86.25 is very similar to that from W86.81, with a constant pattern speed and a perturbation amplitude that shows an artificial trend over time due to an inappropriate damping model. The peak signal associated with W86.25 is around $70 \text{ cm}^2 \text{ s}^{-2}$, and therefore is a bit below that of W86.81 and a bit above that of W86.79. By contrast, the signal from W86.18 is near the limit of detection at $50 \text{ cm}^2 \text{ s}^{-2}$, and is only clearly detected in the Epoch 2 data. These data therefore only provide marginal evidence for this particular signal. Follow-up examinations of stellar occultations involving the star α Orionis that have high signal-to-noise in the low optical depth regions outside of the plateaux¹⁰ also reveal a weak wave signal at this location. This suggests that this is probably a real ring feature that could be better

quantified with a future dedicated analysis of only the occultations with the best signal-to-noise in these regions.

Finally, Figure 28 shows a clear signal at $842^{\circ}0 \text{ day}^{-1}$ located around 84,260 km, interior to the innermost plateau (P5) in Figure 17, which we designate W84.26. This pattern has a consistent perturbation amplitude of $80 \text{ cm}^2 \text{ s}^{-2}$, but in this case the variations in the perturbation amplitude over time are more consistent with each other. This suggests that this is probably a transient perturbation that appeared in the late 1990s and reached its peak strength around 2005, before decaying away.

5. Discussion

The above analysis documents the history of multiple anomalies in Saturn's gravitational field with a range of different amplitudes and pattern speeds. Figure 29 provides a high-level summary of the $m = 3$ perturbations, and compares these to Saturn's observed winds, critical times in Saturn's seasonal cycle, and the rotation rates of two major storms observed to have formed in 1990 and 2010. The similarity of the pattern speeds of the $m = 3$ perturbations to the range of rotation rates associated with Saturn's winds still supports the idea that something inside Saturn is producing these gravitational anomalies. Furthermore, the observed variations in the amplitudes and/or pattern speeds of the perturbations over timescales of years to decades suggests that these gravitational anomalies are generated by transient phenomena inside the planet. Possible sources of these gravitational anomalies include localized atmospheric structures like storms or vortices carried around by Saturn's winds and more global oscillations and waves that propagate sufficiently slowly in a frame rotating with the planet. However, there are still substantial uncertainties regarding both the magnitudes and the temporal variability of the gravitational anomalies associated with either of these structures, and detailed modeling of these phenomena is beyond the scope of this report. Instead, we will simply

¹⁰ The high signal-to-noise in these regions was due to the occultations occurring at low ring opening angles (Nicholson et al. 2020). Unfortunately, this also meant that the plateaux were nearly opaque during these occultations, so they could not be included in the full wavelet analysis.

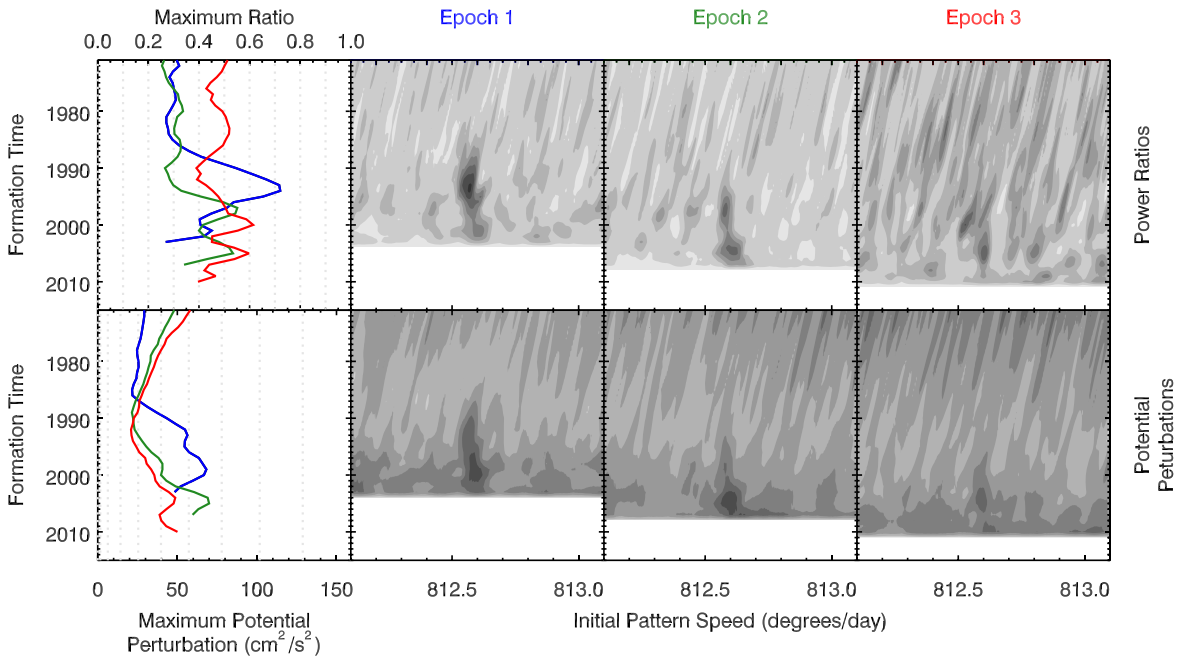


Figure 26. The results of the wavelet analysis of the wave W86.25 in the same format as Figure 15. This region contains a wave signal with a pattern speed of around 812.6 day^{-1} during all three epochs.

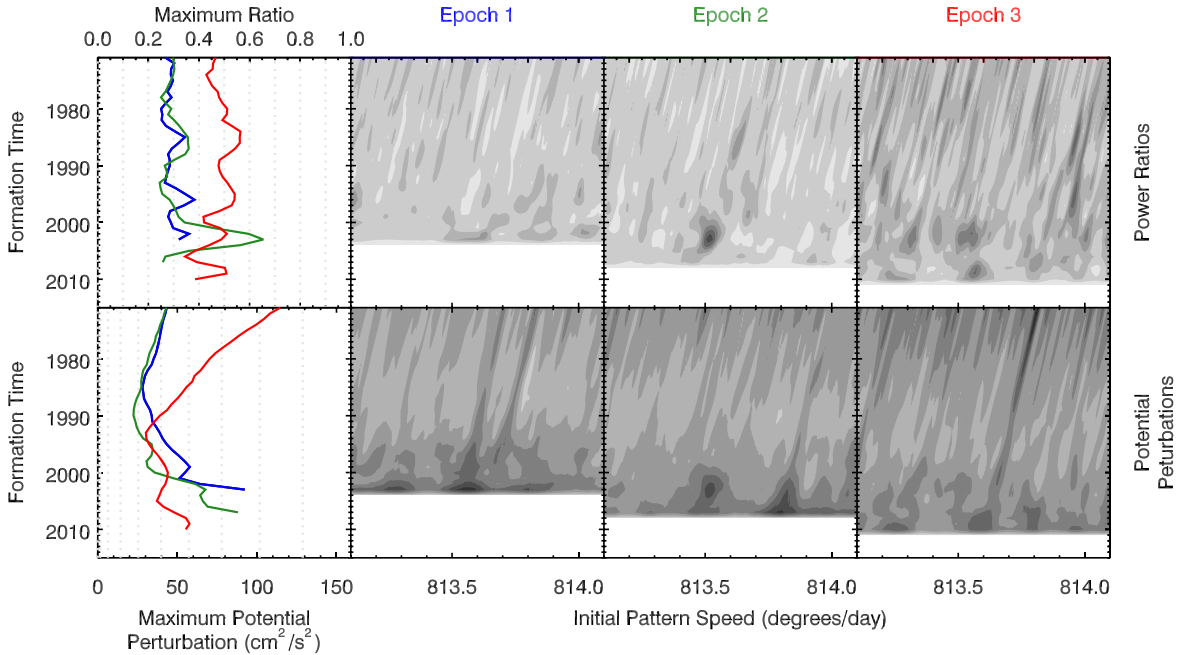


Figure 27. The results of the wavelet analysis of the wave W86.18 in the same format as Figure 15. This region contains a weak wave signal with a pattern speed of around 813.5 day^{-1} , which is most obvious in the Epoch 2 data.

highlight aspects of the observed amplitudes and rotation rates that will be useful for such efforts. In addition, we will discuss how the observed connections between the W86.40 and W85.67 waves indicate that one of the structures inside the planet may be modulated by solar tides.

5.1. Amplitudes

The gravitational anomalies required to produce the waves examined here are not the strongest anomalies in the planet’s gravitational field. The gravitational potential perturbations required to produce the observed wave signatures are between

50 and $150 \text{ cm}^2 \text{ s}^{-2}$. These potentials would produce accelerations near Saturn’s surface of order $\Phi'_m/R_s = 0.8\text{--}2.5 \times 10^{-10} \text{ m s}^{-2}$. This is orders of magnitude less than the $\sim 10^{-6} \text{ m s}^{-2}$ unexplained variations in the accelerations experienced by the Cassini spacecraft during its multiple close passages by Saturn (Iess et al. 2019), and is much smaller than the $\sim 5 \times 10^{-8} \text{ m s}^{-2}$ variations seen in the accelerations of the Juno spacecraft, which might reflect storms or oscillations inside Jupiter (Durante et al. 2020). Thus, these anomalies are only responsible for a small fraction of the structure in Saturn’s gravitational field.

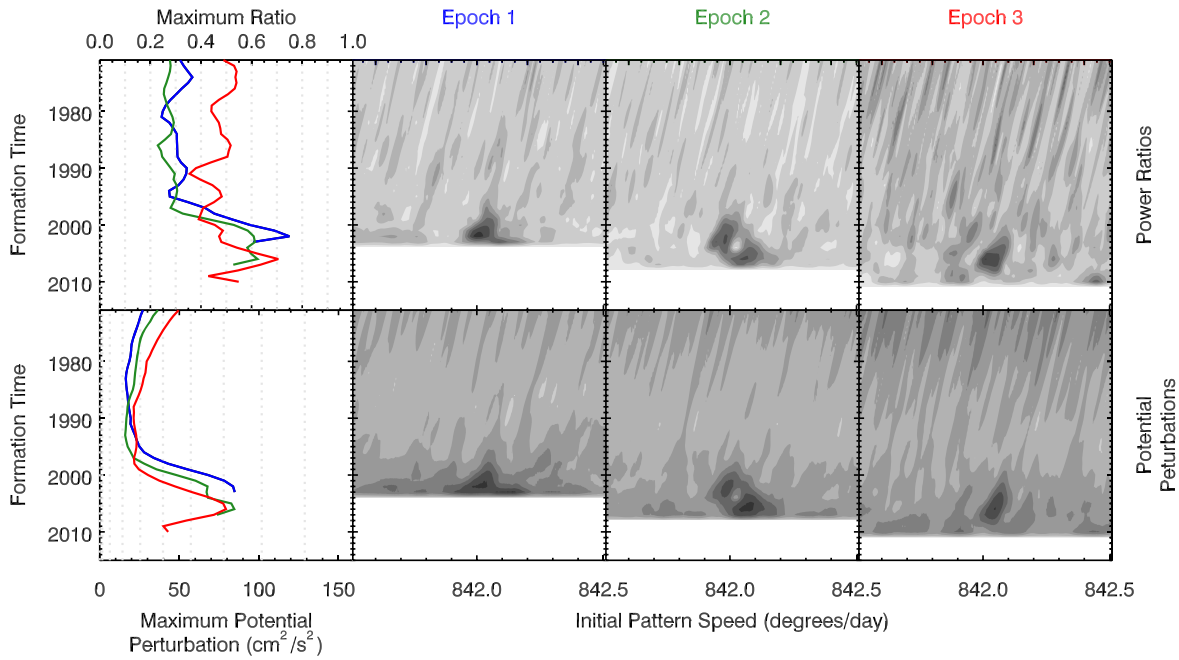


Figure 28. The results of the wavelet analysis of the wave W84.26 in the same format as Figure 15. This region contains a wave signal at $842^\circ \text{ day}^{-1}$. Note that unlike the other signals outside the plateaux, the signal is consistently found only after 2000.

If these anomalies were due to compact regions of enhanced density carried around by Saturn’s winds, then the total mass of these regions would be of order $\Phi'_m R_S / G$ (see Equation (62) above), which for $\Phi'_m = 100 \text{ cm}^2 \text{ s}^{-2}$ is only around 10^{15} kg (comparable to an icy satellite with a diameter of about 10 km). This is consistent with prior estimates (Hedman & Nicholson 2014), but it is not yet clear whether such a mass enhancement could be supported inside a fluid planet like Saturn. Indeed, recent work has shown that the gravitational signatures of large storms are better modeled as a dipolar density anomaly consisting of an overdense region sitting on top of an underdense region (Parisi et al. 2020, 2021). The gravitational potential perturbation generated by such a system would be of order $G d_M / R_S^2$, where d_M is the mass dipole moment associated with the storm. Producing a potential perturbation of order $100 \text{ cm}^2 \text{ s}^{-2}$ would require a structure with a dipole moment of order $5 \times 10^{23} \text{ kg m}$. This is the same order of magnitude as a recent estimate of the dipole moment of Jupiter’s Great Red Spot, based on the observed accelerations of the Juno Spacecraft as it flew over that storm (Parisi et al. 2021). This may mean that storms in Saturn’s atmosphere could potentially generate at least some of the waves in the rings, although further work is needed to ascertain whether it is likely that suitably intense and deep storms exist in Saturn.

Alternatively, these gravitational waves could be generated by global oscillations with suitably strong $m = 3$ components and pattern speeds close to the planet’s bulk rotation rate. Giant planets are expected to have a complex spectrum of inertial and/or gravito-inertial modes with suitable pattern speeds that are currently being investigated in part because of their potential effects on giant planets’ tidal response and dissipation (Barker et al. 2016; Fuller et al. 2016; Ogilvie 2020; Lin & Ogilvie 2021).¹¹ These structures may even exhibit some

amount of time variability similar to the observed gravitational anomalies (Barker & Lithwick 2013; Barker 2016). However, in order for these sorts of global oscillations to produce detectable ring waves, they would have to generate perturbations in the planet’s gravitational potential comparable to those associated with the fundamental normal modes or mixed fundamental and gravitational normal modes responsible for several other waves in the C ring (Fuller 2014; Hedman & Nicholson 2014; French et al. 2016; Hedman & Nicholson 2016; Dewberry et al. 2021; Mankovich & Fuller 2021). While the relative amplitudes of the various modes inside giant planets is currently an active area of research (Wu 2005; Markham & Stevenson 2018; Wu & Lithwick 2019; Markham et al. 2020; Lin & Ogilvie 2021; Dewberry & Lai 2022), we are not aware of any explicit predictions for the likely range of gravitational signals generated by oscillations with the pattern speeds of the waves considered here. We therefore expect that additional work will be needed to ascertain whether any of these oscillations could produce these waves.

Another way of determining whether these gravitational anomalies are due to localized atmospheric features or global oscillations is by comparing the strengths of gravitational perturbations with different m -values. Global oscillations can produce signals with a single azimuthal wavenumber, but mass anomalies carried around by Saturn’s winds produce gravitational perturbations similar to orbiting satellites, and so should generate a series of waves with predictable locations and relative amplitudes (El Moutamid et al. 2016). While there are hints of wave signals near some of these predicted locations, it is not yet practical to use these potential signals to help constrain the sources of the relevant gravitational perturbations, because the vast majority of these waves generated by localized atmospheric features should occur in the A and B rings. These rings have much higher surface mass densities than the C ring, which makes identifying these waves more difficult, because it reduces their amplitudes and enhances offsets in their pattern

¹¹ Rossby waves with $m = 3$ have also been observed in Saturn’s stratosphere (Guerlet et al. 2018), but those structures do not involve enough material to generate sufficiently strong gravitational perturbations.

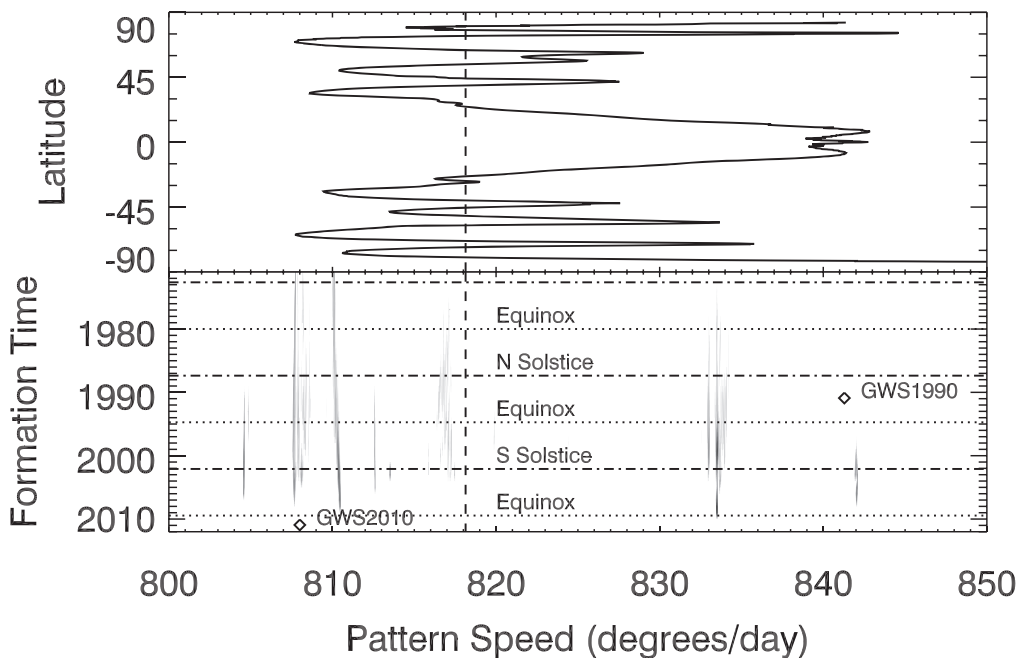


Figure 29. A summary of the history of the anomalies in Saturn’s gravitational field, compared with notable aspects of Saturn’s atmosphere and seasons. The top panel shows the rotation rates of Saturn’s winds, using data from García-Melendo et al. (2011). The bottom panel shows a grayscale map of the average perturbations in Saturn’s gravitational field as a function of pattern speed and formation time. For the sake of clarity, signals are only shown where the average power ratio is above a time-dependent threshold (0.35 before 2004, 0.5 between 2004 and 2008, and 0.7 between 2008 and 2011). The vertical dashed line is the estimate of Saturn’s interior rotation rate by Mankovich et al. (2019), while the diamonds mark the rotation rates of notable Saturn storms known as “Great White Spots” (Sánchez-Lavega et al. 2018). The horizontal lines mark Saturn’s solstices and equinoxes.

speeds. Furthermore, the B ring is nearly opaque, while the A ring contains many satellite-driven density waves, both of which complicate isolating the appropriate wave signals. Comparing any potential wave signals with the C ring structures considered here is therefore a nontrivial task that will likely be a productive avenue for future work.

5.2. Pattern Speeds

Turning to the pattern speeds of the signals, it is important to first note that correlating the overall distribution of the gravitational signatures with aspects of Saturn’s visible atmosphere is challenging, because the detectability of gravitational anomalies depends on local ring properties, with the plateaux apparently being better able to preserve weaker signals over a longer period of time than other parts of the rings. Nevertheless, given that the strongest signals both inside and outside the plateaux correspond to potential perturbations around $100 \text{ cm}^2 \text{ s}^{-2}$, Figure 29 most likely provides a reasonably complete survey of those particular gravitational anomalies for the time period between 1995 and 2010, and a more patchy history of weaker signatures.

At first, the overall similarity of the distribution of the gravitational anomaly pattern speeds to the rotation rates of Saturn’s winds looks like it would strongly support the idea that these gravitational signals come from localized atmospheric phenomena like storms. However, closer inspection reveals that there is surprisingly little correlation between these strong anomalies in the planet’s gravitational field and the most dramatic storms observed in its clouds.

While Saturn’s visible cloud structures are usually relatively subdued compared to Jupiter’s, roughly once each Saturn year there is a major event that produces large atmospheric disturbances known as Great White Spots, two of which have

occurred in the last 40 yr (Sánchez-Lavega et al. 2018). One appeared in Saturn’s equatorial jet in 1990, while the other appeared at mid-northern latitudes in late 2010 (Sánchez-Lavega et al. 2018). Given that these are the most obvious events in Saturn’s atmosphere over the past 40 yr, one might naturally expect that they would produce strong gravitational signatures, but this does not seem to be the case.

There is no obvious signature of the 1990 event in the rings. This discrepancy could potentially be explained by the fact that the wave generated by this event would have occurred outside of any plateaux. In these regions, even relatively strong waves seem to fade away when they are more than 20 yr old, likely due to enhanced dissipation rates. The signal from the 1990 event might therefore have damped away before Cassini was able to observe it.

The rotation rates of various components of the 2010 giant storm were between 808° and $810^\circ \text{ day}^{-1}$ (Sánchez-Lavega et al. 2018), which is close to two of our strongest waves. However, attributing either of these gravitational field anomalies to the 2010 event is difficult, because this region contains multiple patterns that have existed since at least 1980, and while the intensity of the pattern at $810.5^\circ \text{ day}^{-1}$ decreased a few years before 2010, and the intensity of the pattern around $808^\circ \text{ day}^{-1}$ might have begun to rise around that time, there are not any obvious dramatic changes in the strengths or locations of these long-lived anomalies that could be attributed to the 2010 event. More detailed modeling of these sorts of outbursts could reveal that the 2010 event was a brief surface manifestation of a deep storm that produced the gravitational asymmetry, but at the moment any connection between the 2010 event and these long-lived gravitational anomalies appears to be indirect.

Besides the lack of obvious correlations with major atmospheric outbursts, it is also worth noting that some of the

gravitational anomaly pattern speeds fall outside the range of rotation rates in Saturn's visible winds. In particular, there are two waves that are generated by perturbations with pattern speeds of around 804.7 day^{-1} (see Section 4.5). These are substantially slower than the lowest rotation rates associated with Saturn's observed winds (García-Melendo et al. 2011), so if they are to be attributed to discrete storms, they would need to be in a deep atmospheric layer with winds that differ substantially from the visible cloud tops.

In this context, it is interesting to note that the anomalies responsible for the observed waves can be divided into two broad classes, based on their appearance in the maps shown in Section 4. One class consists of relatively transient features lasting less than a decade (like the ones around $833^\circ \text{ day}^{-1}$), with the other containing more persistent anomalies that appear to last for several decades (like the ones at 807.6° and $810^\circ \text{ day}^{-1}$). Of course, such a classification is more challenging to apply to weaker features, but we can note that all of the signals with pattern speeds above $815^\circ \text{ day}^{-1}$ appear to be transient. By contrast, for pattern speeds below $815^\circ \text{ day}^{-1}$, clearly transient signals are only found between 807.6° and $808.5^\circ \text{ day}^{-1}$ (see Figure 23). The rest of the signals are either certainly long-lived (e.g., the ones at 807.5° and $810^\circ \text{ day}^{-1}$) or are potentially long-lived features found outside the plateaux (e.g., the signals around 805° and $813^\circ \text{ day}^{-1}$, although difficulties in properly modeling the wave dissipation in these regions makes this identification less certain).

Interestingly, the distribution of transient features between 808° and $842^\circ \text{ day}^{-1}$ matches the range of rotation rates seen in Saturn's visible winds. By contrast, the more persistent patterns all have pattern speeds substantially less than the planet's bulk rotation rate of $818^\circ \text{ day}^{-1}$ (Mankovich et al. 2019). This could indicate that the transient features are due to relatively shallow atmospheric phenomena that are carried around the planet at roughly the same rate as the visible winds, while the more persistent features are from a deeper layer whose dynamics and rotation state are distinct from the visible clouds. Such a finding might be consistent with recent measurements of the static gravity field that indicate the planet contains a subcorotating region at moderate depths (Iess et al. 2019), but much more work is needed to rigorously evaluate this idea. Alternatively, the longer-lived structures could represent global oscillations with pattern speeds that are slightly slower than the planet's bulk rotation rate, such as inertial and gravito-inertial waves (Barker et al. 2016; Ogilvie 2020; Lin & Ogilvie 2021; Saio et al. 2021).

We can also note that the variations in both the amplitudes and pattern speeds of these gravitational anomalies provide yet another means of better constraining their origins. On Jupiter, both the sizes and drift rates of long-lived storms like the Great Red Spot have been observed to change over timescales of years to decades (Simon et al. 2018; Barrado-Izaguirre et al. 2021; Wong et al. 2021; Morales-Juberías et al. 2022), and the variations in these storms' drift rates around the planet are even comparable to those found in Saturn's gravitational anomalies. Detailed examinations of the evolution of the structures in Saturn's atmosphere over the course of the Cassini Mission and beyond could therefore potentially reveal features with histories that match some of the signals identified in this work.

5.3. The $m = -1$ Wave and a Potential Connection with Solar Tides

The previous discussion has focused on the $m = 3$ patterns, but we should not forget that the persistent $m = 3$ feature with a

pattern speed of around $810^\circ \text{ day}^{-1}$ appears to be associated with an $m = -1$ anomaly rotating three times faster. Since this is the only $m = 3$ wave with an $m = -1$ companion, this anomaly is likely to be a special case. A full understanding of these waves will likely require detailed dynamical models of the planet's interior that are beyond the scope of this paper. However, comparing the terms in the gravitational potential required to produce these two waves suggests that solar tides could be playing an important role.

To illustrate why tidal processes could be relevant to this system, let us focus on a scenario where the $m = 3$ waves are generated by compact storms carried around by Saturn's winds. Recall that each wave is generated by a specific term in the gravitational expansion with the form $\cos(|m|(\lambda - \Omega_p t))$. Hence, the $m = 3$ wave requires a term in the gravitational potential that goes like $\cos(3\lambda - 3\Omega_3 t)$ with $\Omega_3 \simeq 810^\circ \text{ day}^{-1}$, while the $m = -1$ wave requires a term that goes like $\cos(\lambda - \Omega_1 t)$ with $\Omega_1 \simeq 2430^\circ \text{ day}^{-1}$. The first term arises naturally if we consider a compact mass M_A moving on a circular trajectory in Saturn's equatorial plane at a radius r_A and a rate Ω_A , because in this case the distance between the mass anomaly and a point in the ring at radius r and inertial longitude λ is

$$d = \sqrt{r_A^2 + r^2 - 2rr_A \cos(\lambda - \Omega_A t)}. \quad (55)$$

The corresponding perturbation to the gravitational potential $\Phi' = GM_A/d$ can therefore be expanded as a power-law series in $\cos(\lambda - \Omega_A t)$ and then rewritten in the following form:

$$\Phi' = \frac{GM_A}{r} \sum_{m=1}^{\infty} f_m(r_A/r) \cos(m(\lambda - \Omega_A t)), \quad (56)$$

where $f_m(r_A/r)$ are functions of the ratio r_A/r that can be expressed in terms of Laplace coefficients. For a mass anomaly carried around by Saturn's winds, Ω_A can easily be around $810^\circ \text{ day}^{-1}$, and so the $m = 3$ term in this expansion goes like $\cos(3\lambda - 3\Omega_A t)$, as desired. Note that if we instead made the anomaly inside the planet a dipole (cf. Parisi et al. 2020, 2021), then M_A would be replaced by the dipole moment of the anomaly divided by r_A , and the f_m functions would be different, but the overall form of the series would be the same. Either of these models therefore naturally produces the term in the potential needed to drive the $m = 3$ wave.

However, the $m = 1$ term in this expansion will go like $\cos(\lambda - \Omega_A t)$, and so the pattern speed of the corresponding wave will be a factor of 3 too small. The $m = -1$ wave therefore cannot be easily explained as the result of a constant mass anomaly moving at a steady rate comparable to the planet's rotation. Instead, we would need a mass anomaly moving around the planet at three times the planet's spin rate, which currently seems unlikely.

Now consider the possibility that as the anomaly moves around the planet, its effective mass M_A (or, equivalently, its dipole moment) can vary with longitude and time. These variations could correspond to oscillations in the storm's vertical position or extent in the planet's atmosphere. In principle, such variations could be arbitrarily complex, but for the sake of simplicity, let us say that they have the following form:

$$M_A = M_0 [1 + \mu_x \cos(m_x(\lambda - \Omega_x t))] \quad (57)$$

for some values of m_x and Ω_x (note that this corresponds to the effective anomaly mass varying with longitude in a frame rotating at the rate Ω_x). In this case, the $m=3$ term in Equation (56) becomes:

$$\begin{aligned} \Phi'_3 = & \frac{GM_0}{r} f_3(r_A/r) \cos(3\lambda - 3\Omega_A t) \\ & + \frac{GM_0 \mu_x}{2r} f_3(r_A/r) \cos((3 + m_x)\lambda - (3\Omega_A + m_x \Omega_x) t) \\ & + \frac{GM_0 \mu_x}{2r} f_3(r_A/r) \cos((3 - m_x)\lambda - (3\Omega_A - m_x \Omega_x) t). \end{aligned} \quad (58)$$

The first term in this expression has the correct form to produce the $m=3$ wave with a pattern speed of Ω_A , while the other two terms will produce waves with different m -numbers and pattern speeds. More specifically, if we let $m_x=2$, then the last term will go like $\cos(\lambda - (3\Omega_A - 2\Omega_x)t)$, and so produce an $|m|=1$ wave with a pattern speed of $3\Omega_A - 2\Omega_x$. Recall that the pattern speed of the $m=-1$ wave is close to three times Saturn's rotation rate, so this term in the potential will naturally generate the desired wave, provided that Ω_x is sufficiently close to zero. Furthermore, slow changes in Ω_A and M_0 will produce the observed coordinated changes in the pattern speeds and amplitudes of the two waves, while slow changes in μ_x allow the relative amplitudes of the two waves to change over time.

At first, it might seem that $m_x=2$ and $2\Omega_x \ll 3\Omega_A$ are rather arbitrary choices, but in fact these particular parameter values correspond to tidal distortions in the structure of the planet. In order to produce an $m=3$ wave with pattern speed Ω_3 and an $m=-1$ wave with pattern speed Ω_1 , we need the magnitude of the mass anomaly to go like:

$$M_A = M_0 [1 + \mu_x \cos(2\lambda - [3\Omega_3 - \Omega_1]t)]. \quad (59)$$

This behavior is reminiscent of tidal phenomena, which have $m=2$ structures that rotate slowly relative to inertial space compared to the planet's spin rate. We therefore may posit that as the anomaly moves around the planet, its amplitude is modified by some aspect of the planet's internal structure that is affected by a tidal force.

We can even ascertain which sort of tidal potential is relevant by evaluating the pattern speed of the tidal term $\Omega_x = (3\Omega_3 - \Omega_1)/2$. From visual inspection of the maps shown in Figures 20 and 21, we can see that this difference is much less than a degree per day, which immediately eliminates tides due to Saturn's major moons, which all move around the planet at speeds of at least several degrees per day. This leaves the Sun as the most likely source of this term, which from Saturn's perspective moves around the planet at only $0^\circ 03 \text{ day}^{-1}$. To see if this rate is consistent with the observed values of Ω_3 and Ω_1 , we found the pattern speeds corresponding to the peak potential perturbation for the $m=3$ signals between 809° and $811^\circ \text{ day}^{-1}$ and the $m=-1$ signals between 2428° and $2432^\circ \text{ day}^{-1}$ for all years between 1996 and 2004 in all three epochs (when all three epochs have decent signal-to-noise and consistent values for $(3\Omega_3 - \Omega_1)/2$). If we assume a surface mass density of 1.3 g cm^{-2} for both waves, then we find that $(3\Omega_3 - \Omega_1)/2$ is around $0^\circ 085 \text{ day}^{-1}$, but this drops to around $0^\circ 050 \text{ day}^{-1}$ if we assume a surface mass density of around 0.7 g cm^{-2} for the $m=-1$ wave, consistent with the observations described above. Besides such systematic uncertainties, the finite widths of the signals in Figures 20 and 21 suggest that

there are additional uncertainties in the individual pattern speeds that are of order $0^\circ 05 \text{ day}^{-1}$. A rigorous examination of these uncertainties is beyond the scope of this report, but even this rough assessment indicates that the observed values of $\Omega_x = (3\Omega_3 - \Omega_1)/2$ appear to be reasonably consistent with that expected for solar tides.

We may therefore suggest that the atmospheric structure responsible for the $810^\circ \text{ day}^{-1}$ wave has been passing through a region of Saturn's atmosphere with a particularly strong response to solar tides, which somehow modulate the magnitude of the gravitational anomaly associated with that structure. The primary challenge for this idea is that the comparable amplitudes of the potential perturbations associated with the $m=3$ and $m=-1$ waves imply that the modulation term μ_x is of order unity. This means that the perturbation responsible for the $m=3$ wave must undergo substantial variations in its effective strength as it moves around the planet and through the tidal bulge. This is not likely to be the case for a simple mass concentration, since it would require the anomaly to gain and lose a substantial amount of mass twice each rotation.

Large changes in the potential perturbation strength could be possible for more complex structures in the planet. For example, consider the dipolar model that has recently been used to model the gravitational perturbations associated with Jupiter's Great Red Spot (Parisi et al. 2020, 2021). This model treats strong storms as a mass excess at one level in the atmosphere some distance above a comparable mass deficit. If we imagine the vertical positions of these two layers changed by different amounts in response to the relevant tidal potential, then the separation between them would change as they move around the planet, which would naturally cause the dipole moment of the anomaly to vary in the appropriate way. The comparable amplitudes of the two ring waves would then require that the variations in the separation between the two mass anomalies be comparable to their average separation. Similar scenarios could potentially also work with more global oscillations involving mass concentrations and deficits at different levels in the atmosphere. In either case, the relevant structure would need to span an atmospheric layer that has a strong gradient in its tidal response, which would most likely involve some sort of resonant interaction with the solar tide similar to those that have been considered in Earth's atmosphere (Zahnle & Walker 1987).

There are two different ways one might attempt to test and further explore this idea. On the one hand, this model does predict that there should be a third term in the gravitational potential of comparable magnitude to the one responsible for the $m=-1$ wave. This term is generated by the middle term in Equation (58), which would produce an $m=5$ perturbation in the gravitational potential with a pattern speed of around $486^\circ \text{ day}^{-1}$, and so generate an $m=5$ wave at around 136,400 km from Saturn's center in the outer A ring. Initial searches of this region found no evidence for such a wave. However, this is a ring region with a much higher surface mass density and many satellite-generated waves, which may obscure this particular wave signal. The tidal term could also potentially interact with other terms in the expansion in Equation (56), producing additional waves that could exist in other ring regions. However, more work is needed to ascertain whether the expected signals from these gravitational perturbations are likely to be detectable in the currently available data.

A potentially more productive approach for testing this idea would involve modeling of the two observable signals and seeing whether they can be generated by realistic atmospheric structures. Recall that only one $m=3$ wave has a corresponding $m=-1$ wave, and the amplitude of the $m=-1$ term appears to have been declining over the past few decades, even as the amplitude of the $m=3$ term has been increasing. According to the above model, this implies that the tidal resonance that generates strong gradients in anomaly separations occurs in a particular part of the atmosphere that is rotating at $810^\circ \text{ day}^{-1}$. It would therefore be worthwhile to determine what properties a layer in Saturn's atmosphere would need to have (e.g., mean density, scale height, rotation rate, and relevant resonance frequencies) in order to produce a tidal resonance at that particular rotation rate and ascertain whether those layers could also support a suitably strong gravitational anomaly. Such studies are likely to provide insights into where these atmospheric structures can be found and what these structures might be.

The authors thank C. Mankovich, J. Fuller, M. Marley, R. French, M. Tiscareno, M. Parisi, A. Simon, and K. Soderlund for helpful discussions. The authors also wish to thank the reviewers for their helpful comments. This work was supported by NASA Cassini Data Analysis Program grants NNX178AF85G and 80NSSC19K0893.

Appendix

Expected Relationships between Wave Amplitudes and Perturbation Strengths

While there is not yet a complete theory for density waves generated by time-variable periodic forces, the theory of linear density waves generated by purely periodic perturbing forces provides useful insights into the relationship between wave amplitudes and gravitational perturbation strengths. For these waves, the asymptotic form of the wave amplitude A in an optical depth profile¹² is typically written in terms of distance from the resonance radius using the following expression (Nicholson et al. 1990; Marley & Porco 1993; Tiscareno & Harris 2018; with the approximation that the local mean motion is $\sqrt{GM_P/r_L^3}$):

$$A(r) = \frac{\Phi'_m}{\pi G \sigma_0 r_L} \sqrt{\frac{3|m-1|M_P}{2\pi\sigma_0 r_L^2}} \frac{(r-r_L)}{r_L} e^{-(r-r_L)^3/r_D^3}, \quad (60)$$

where σ_0 is the local ring surface mass density, r_L is the resonant radius, r_D is the characteristic damping length of the wave, and Φ'_m is the effective gravitational potential perturbation acting on the ring. Note that this potential is often expressed in terms of a normalized torque from the resonance T/σ_0 using the relationship

$$\Phi'_m = \sqrt{\frac{3|m-1|n_L^2 \mathcal{T}}{m\pi^2 \sigma_0}}. \quad (61)$$

For a first-order resonance with a satellite of mass M_s with semimajor axis a_s , the perturbing potential is given by the

expression (Nicholson et al. 1990)

$$\Phi'_m = \sqrt{\pi} \frac{GM_s}{a_s} \left[\alpha \frac{db_{1/2}^m}{d\alpha} + 2mb_{1/2}^m \right], \quad (62)$$

where $\alpha = r_L/a_s$ and $b_{1/2}^m(\alpha)$ is a Laplace coefficient (Shu 1984; Murray & Dermott 1999). Expressions of a similar form can be obtained for higher-order satellite resonances (Tiscareno & Harris 2018). Meanwhile, for a standard planetary normal mode of degree ℓ and azimuthal wavenumber m (Marley & Porco 1993),

$$\Phi'_m = (2m + \ell + 1)\Phi'_{\ell m}, \quad (63)$$

where $\Phi'_{\ell m}$ is the relevant component of the planet's gravitational potential due to that normal mode.

Equation (60) can be recast in terms of elapsed time $\delta t = (r - r_L)/v_g$, making the further approximation that $\kappa_L \simeq \sqrt{GM_P/r_L^3}$. This yields the following expression:

$$A(r) = \Phi'_m \sqrt{\frac{3|m-1|}{2\pi G \sigma_0 r_L^3}} \delta t e^{-\delta t^3/t_D^3}, \quad (64)$$

where t_D is a characteristic damping time that depends on the ring's kinematic viscosity ν as follows (Shu 1984; Tiscareno et al. 2007):

$$t_D = \left(\frac{8r_L^2 \kappa_L^2}{7|m-1|^2 \nu m_L^4} \right)^{1/3}. \quad (65)$$

The amplitude of the wave is therefore proportional to Φ'_m for all elapsed times or wavenumbers, with a constant of proportionality that is a function of δt and depends upon σ_0 , t_D , and $|m-1|$. Note that for both the $m=3$ and $m=-1$ waves considered here, $|m-1|=2$, so the amplitude evolution of both types of wave fragments should be comparable to each other in regions with similar σ_0 and ν . This is why the satellite-driven waves with $m=3$ can be used to estimate the conversion factors for all of the waves of interest to this study.

ORCID iDs

M. M. Hedman  <https://orcid.org/0000-0002-8592-0812>
P. D. Nicholson  <https://orcid.org/0000-0003-2275-4463>
M. El Moutamid  <https://orcid.org/0000-0002-4416-8011>

References

- Acton, C. H. 1996, *PSS*, 44, 65
Baillié, K., Colwell, J. E., Lissauer, J. J., Esposito, L. W., & Sremčević, M. 2011, *Icar*, 216, 292
Barker, A. J. 2016, *MNRAS*, 459, 939
Barker, A. J., Braviner, H. J., & Ogilvie, G. I. 2016, *MNRAS*, 459, 924
Barker, A. J., & Lithwick, Y. 2013, *MNRAS*, 435, 3614
Barrado-Izagirre, N., Legarreta, J., Sánchez-Lavega, A., et al. 2021, *Icar*, 361, 114394
Brown, R. H., Baines, K. H., Bellucci, G., et al. 2004, *SSRv*, 115, 111
Colwell, J. E., Cooney, J. H., Esposito, L. W., & Sremčević, M. 2009, *Icar*, 200, 574
Dewberry, J. W., & Lai, D. 2022, *ApJ*, 925, 124
Dewberry, J. W., Mankovich, C. R., Fuller, J., Lai, D., & Xu, W. 2021, *PSJ*, 2, 198
Durante, D., Parisi, M., Serra, D., et al. 2020, *GeoRL*, 47, e86572
El Moutamid, M., Nicholson, P. D., Hedman, M. M., et al. 2016, AAS/ Division of Dynamical Astronomy Meeting, 47, 400.05
French, R. G., Bridges, B., Hedman, M. M., et al. 2021, *Icar*, 370, 114660
French, R. G., McGhee-French, C. A., Lonergan, K., et al. 2017, *Icar*, 290, 14

¹² Note that this is different from the wavelet amplitude signal A_w , which depends on both radius and wavenumber.

- French, R. G., McGhee-French, C. A., Nicholson, P. D., & Hedman, M. M. 2019, *Icar*, **319**, 599
- French, R. G., Nicholson, P. D., Hedman, M. M., et al. 2016, *Icar*, **279**, 62
- Fuller, J. 2014, *Icar*, **242**, 283
- Fuller, J., Luan, J., & Quataert, E. 2016, *MNRAS*, **458**, 3867
- García-Melendo, E., Pérez-Hoyos, S., Sánchez-Lavega, A., & Hueso, R. 2011, *Icar*, **215**, 62
- Guerlet, S., Fouchet, T., Spiga, A., et al. 2018, *JGRE*, **123**, 246
- Hedman, M. M., & Nicholson, P. D. 2013, *AJ*, **146**, 12
- Hedman, M. M., & Nicholson, P. D. 2014, *MNRAS*, **444**, 1369
- Hedman, M. M., & Nicholson, P. D. 2016, *Icar*, **279**, 109
- Hedman, M. M., Nicholson, P. D., & French, R. G. 2019, *AJ*, **157**, 18
- Iess, L., Militzer, B., Kaspi, Y., et al. 2019, *Sci*, **364**, aat2965
- Jacobson, R. A., Spitale, J., Porco, C. C., et al. 2008, *AJ*, **135**, 261
- Lin, Y., & Ogilvie, G. I. 2021, *ApJL*, **918**, L21
- Mankovich, C., & Fuller, J. 2021, *NatAs*, **5**, 1103
- Mankovich, C., Marley, M. S., Fortney, J. J., & Movshovitz, N. 2019, *ApJ*, **871**, 1
- Markham, S., Durante, D., Iess, L., & Stevenson, D. 2020, *PSJ*, **1**, 27
- Markham, S., & Stevenson, D. 2018, *Icar*, **306**, 200
- Marley, M. S., & Porco, C. C. 1993, *Icar*, **106**, 508
- Morales-Juberías, R., Simon, A. A., & Cosentino, R. G. 2022, *Icar*, **372**, 114732
- Murray, C. D., & Dermott, S. F. 1999, *Solar System Dynamics* (Cambridge: Cambridge Univ. Press)
- Nicholson, P. D., Ansty, T., Hedman, M. M., et al. 2020, *Icar*, **344**, 113356
- Nicholson, P. D., Cooke, M. L., & Pelton, E. 1990, *AJ*, **100**, 1339
- Ogilvie, G. 2020, in *Fluid Mechanics of Planets and Stars*, ed. L. D. Le Bars (Cham: Springer), 1
- Parisi, M., Folkner, W. M., Galanti, E., et al. 2020, *P&SS*, **181**, 104781
- Parisi, M., Kaspi, Y., Galanti, E., et al. 2021, *Sci*, **374**, 964
- Rosen, P. A., Tyler, G. L., Marouf, E. A., & Lissauer, J. J. 1991, *Icar*, **93**, 25
- Saio, H., Takata, M., Lee, U., Li, G., & Van Reeth, T. 2021, *MNRAS*, **502**, 5856
- Sánchez-Lavega, A., Fischer, G., Fletcher, L. N., et al. 2018, in *Saturn in the 21st Century*, ed. K. H. Baines et al. (Cambridge: Cambridge Univ. Press), 377
- Shu, F. H. 1984, in *Planetary Rings*, ed. R. Greenberg & A. Brahic (Tucson, AZ: Univ. Arizona Press), 513
- Simon, A. A., Tabataba-Vakili, F., Cosentino, R., et al. 2018, *AJ*, **155**, 151
- Tiscareno, M. S., Burns, J. A., Nicholson, P. D., Hedman, M. M., & Porco, C. C. 2007, *Icar*, **189**, 14
- Tiscareno, M. S., & Harris, B. E. 2018, *Icar*, **312**, 157
- Tiscareno, M. S., & Hedman, M. M. 2018, *RSPTA*, **376**, 20180046
- Tiscareno, M. S., Nicholson, P. D., Burns, J. A., Hedman, M. M., & Porco, C. C. 2006, *ApJL*, **651**, L65
- Torrence, C., & Compo, G. P. 1998, *BAMS*, **79**, 61
- Wong, M. H., Marcus, P. S., Simon, A. A., et al. 2021, *GeoRL*, **48**, e93982
- Wu, Y. 2005, *ApJ*, **635**, 674
- Wu, Y., & Lithwick, Y. 2019, *ApJ*, **881**, 142
- Zahnle, K., & Walker, J. C. G. 1987, *PreR*, **37**, 95